Available online at www.sciencedirect.com
ScienceDirect
Polymer 49 (2008) 643–675
polymer
www.elsevier.com/locate/polymer

Feature Article

NEXAFS microscopy and resonant scattering: Composition and orientation probed in real and reciprocal space

Harald Ade [a,*], Adam P. Hitchcock [b,**]

[a] Department of Physics, North Carolina State University, Raleigh, NC 27695, USA
[b] Brockhouse Institute for Materials Research, Department of Chemistry, McMaster University, Hamilton, ON, Canada L8S 4M1

Received 29 June 2007; received in revised form 7 October 2007; accepted 20 October 2007
Available online 24 October 2007

Abstract

Near Edge X-ray Absorption Fine Structure (NEXAFS) spectromicroscopy, resonant scattering and resonant reflectivity are specialized, synchrotron radiation based, soft X-ray characterization tools that provide moiety-specific contrast and either real-space imaging at ~30 nm spatial resolution, or scattering signals which can be inverted to provide chemically sensitive information at an even higher spatial resolution (<5 nm). These X-ray techniques complement other real and reciprocal space characterization tools such as various microscopies and conventional electron, X-ray and neutron scattering. We provide an overview of these synchrotron based tools, describe their present state-of-the-art and discuss a number of applications to exemplify their unique aspects.

Keywords: X-ray microscopy; NEXAFS; Resonant scattering; Polymers; Chemical mapping

1. Introduction

Macromolecules can have complicated chemical sequences and internal structures and can assemble into multi-hierarchical, complex assemblies. Biomacromolecules, such as proteins, are excellent examples. Even binary mixtures of homopolymers with simple repeat units quite frequently phase-separate in the melt or in the presence of solvents [1]. Complex morphologies can form during this phase-separation process, particularly in the presence of shear or in thin films [2,3]. Mixtures of various homopolymers in the presence of amphiphiles or block copolymers, or even just block copolymers themselves, also produce a wide range of intricate structures and morphologies [4,5]. This ability of macromolecules to form a range of structure and functionality naturally leads to a wide range of phenomena and technological applications. These applications include multicomponent structural composites as well as self-assembly and directed self-assembly used to template substrates at the nanoscale [6–8]. Consequently, a wide range of analysis methods are employed for the characterization of macromolecules and derivative structures, ranging from spectroscopy to mechanical analysis and neutron scattering [9,10]. Some of these methods require equipment that can be found in the laboratories of individual groups; others, such neutron scattering and reflectivity, require large, shared national or international facilities.

A large number of characterization tools that provide the often required spatial information can be categorized and grouped into:

- microscopies, which directly acquire information in real space;
- diffraction, scattering, and reflectivity techniques, which acquire data in reciprocal space, with real-space information extracted through a mathematical inversion or through model simulations;
- spectroscopies, which typically characterize atomic, molecular or solid state structure, with an interpretation based on reference databases, simulations or quantum computations.

* Corresponding author. Tel.: +1 919 1551 1331.
** Corresponding author. Tel.: +1 905 525 9140x24279.
E-mail addresses: harald_ade@ncsu.edu (H. Ade), aph@mcmaster.ca (A.P. Hitchcock).

0032-3861
doi:10.1016/j.polymer.2007.10.030

Typically, spectroscopies provide information on the smallest length scale, whereas microscopies and scattering typically provide information on the mesoscopic length scale. New and enhanced characterization capabilities result when spectroscopic capabilities, i.e. atomic or near atomic information, can be coupled to either real-space techniques (spectromicroscopy) or reciprocal space techniques (''spectroscattering''). These combinations typically provide quantitative analytical capabilities at the mesoscopic length scale. In this overview, we focus on two such combinations: Soft X-ray Near Edge X-ray Absorption Fine Structure (NEXAFS) microscopy [11,12] and Resonant Soft X-ray Scattering (RSoXS) (for simplicity, we will consider Resonant Soft X-ray Reflectivity (RSoXR), a special application geometry of RSoXS) [13–15]. The former has been developed into a powerful polymer characterization tool over the past 10–15 years. The first realization of the latter method was achieved in the late 1980s [16–19]. Its present implementation at lower photon energy and with substantially more exquisite compositional sensitivity is a rather recent development [13–15]. NEXAFS microscopy and RSoXS are methods that combine atomic and molecular specific soft X-ray spectroscopy [20] with real-space and reciprocal space techniques, respectively. The joining of spectroscopy with microscopy is often referred to as ''spectromicroscopy'', whereas the adjectives ''anomalous'' or ''resonant'' are used to qualify reciprocal space X-ray methods when they provide at least elemental sensitivity and contrast.

The unique abilities of X-ray spectromicroscopy and resonant scattering are based on the specific interactions of soft X-rays with macromolecules. The most basic aspects can be summarized as follows. The various functional groups found in polymers have unique spectral features at their inner shell absorption edges, particularly the C 1s edge ($\sim$290 eV), and, if present, also the N 1s edge ($\sim$405 eV), O 1s edge ($\sim$535 eV), and those of other hetero-atoms. Synchrotron light can be tuned to or scanned over these spectral features while recording high resolution images (NEXAFS microscopy), or while recording scattering patterns (Resonant Soft X-ray Scattering and Resonant Soft X-ray Reflectivity). These photon energy-dependent images or scattering patterns can then be analyzed to give quantitative, spatially resolved chemical information.

With the appropriate X-ray or electron optics, compositional imaging at relatively high spatial resolution ($\sim$30 nm) is possible [21]. Compositional sensitivity and contrast for these real-space techniques are based on absorption and thus the ability to differentiate various materials is reflected in their relative NEXAFS spectra. For scattering, spatial information content can extend to the $\lambda/2$ limit in a backscattering geometry (λ = wavelength, 4.3 nm at C 1s edge) [22,23]. For hard X-rays, scattering intensity is determined by electron density differences between constituent phases. For polymeric materials, the electron density contrast is often low, requiring powerful sources, relatively long acquisition times, or specialized analysis [24]. For enhanced and selective contrast, neutron scattering is often employed, taking advantage of the large difference in scattering length density between hydrogen and deuterium and by selectively deuterating desired functional groups or phases [25,26]. In contrast, RSoXS and RSoXR can achieve improved chemical differentiation relative to conventional X-ray methods and without the need for deuteration though the use of tunable X-ray sources and exploitation of moiety-specific X-ray interactions with the sample near absorption edges [13–16,18,27,28]. Resonant X-ray methods can thus offer important advantages at high spatial resolution for the differentiation of phases in soft condensed matter materials or for thin film analysis [13–15].

Our intent in this manuscript is to provide a somewhat self-contained ''tutorial'' about the methods that includes some practical information that will be useful to new practitioners, along with a set of representative applications that will delineate the capabilities and range of these methods. We first review the operating principles and underlying physics of X-ray spectromicroscopy and the X-ray resonance techniques and then detail some of their technical aspects. We subsequently exemplify the range of possibilities by selectively reviewing some applications. A short summary of the work not detailed in this selective overview is provided in Appendix A to provide a relatively complete review and to mention all the applications to date.

We start with an example to showcase the capabilities of spectromicroscopy. We consider the characterization of a $\sim$150 nm thick film of a blend of poly(9,9-dioctylfluorene-*co*-*N*-(4-butylphenyl)diphenylamine) (TFB) and poly-(9,9′-dioctylfluorene-*co*-benzothiadiazole) (F8BT) spun-cast from a solvent – materials and preparation methods used for the production of experimental organic light emitting diodes (OLEDs) [29]. The NEXAFS spectra from neat TFB and F8BT and compositional maps of F8BT for the blend are shown in Fig. 1a and b, respectively. The corresponding Scanning Probe Microscopic (SPM) image that maps total film thickness is included for comparison as given in Fig. 1c. The spectral differences between TFB and F8BT are relatively large, even though superficially, similar chemical functional groups are present in both materials. In the F8BT-rich region, the F8BT concentration near the domain interface is >90 wt% (Fig. 1a) and falls to $\sim$60 wt% further into the domain. This quantitative composition gradient was used to help explain the relatively efficient performance of TFB:F8BT-based OLEDs [29] (for more details, see the more extensive discussion below). Only the combination of spectroscopy with high spatial resolution microscopy allowed the acquisition of information that provided quantitative compositional maps at the required spatial scale.

Prior reviews of NEXAFS microscopy and its utilization in polymer science include reviews by Ade et al. [30,31], and Ade and Urquhart [32]. General reviews on X-ray microscopy can be found by Kirz et al. [33] and Howells et al. [34]. RSoXS of macromolecular materials using low Z-element absorption edges is a very nascent field and the information provided here is the first comprehensive perspective of these recent developments.

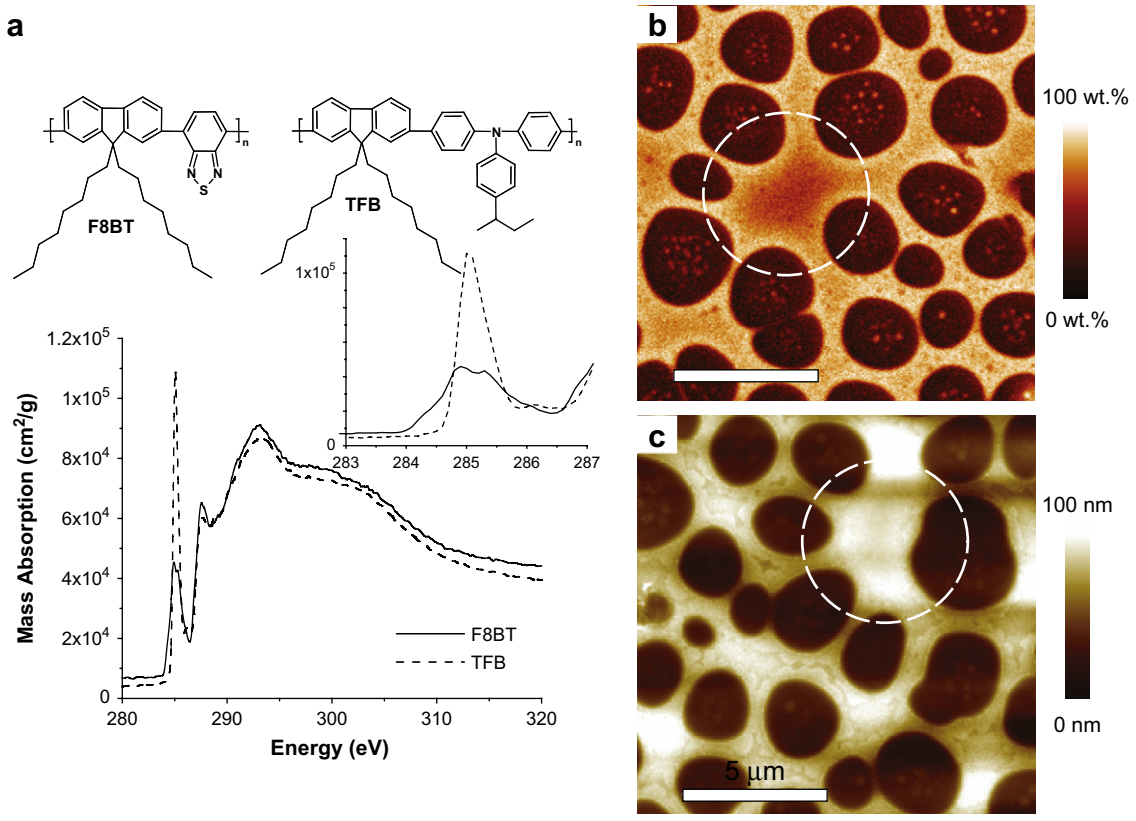

Fig. 1. (a) Chemical structures of F8BT and TFB along with their NEXAFS spectra, (b) 15 μm × 15 μm F8BT compositional map and (c) SPM thickness image of a nominally 150 nm thick blend film. The wider F8B-rich areas highlighted by the circles show little variation in surface features (c) yet a marked decrease in F8BT concentration (b) [29]. (Figure courtesy of McNeill.)

2. Interaction of soft X-rays with matter

2.1. General aspects of X-ray–matter interactions

Soft X-rays cover photon energies, E, from ~50 to ~2000 eV, corresponding to wavelengths λ from ~25 to ~0.62 nm, with λ (nm) = 1239.9/E (eV). In this range, electromagnetic radiation undergoes two types of basic interactions with atoms: scattering and photoabsorption/ionization (conventionally called the 'photoelectric effect') [35]. In this energy range, the probability of absorption is much higher than that for scattering. Furthermore, only elastic scattering (also called coherent scattering) needs to be considered, since the probability of inelastic X-ray scattering, i.e. Compton scattering (also called incoherent scattering), is negligible for soft X-rays. These two basic atomic interactions are often expressed quantitatively in terms of the complex atomic scattering factor $f = f_1 + \mathrm{i}f_2$. In the long wavelength limit, i.e. for wavelengths λ that are large compared to the Bohr radius a_0 or the dimension of the atoms, as well as in the small angle limit (forward scattering), f turns into an angle independent (forward) scattering factor $f^0 = f_1^0 + \mathrm{i}f_2^0$ [36]. In the long wavelength limit relevant here, there is no distinction between f and f^0, and we will use f for simplicity. Furthermore, the interaction of X-rays with matter can also be described using the complex index of refraction $n = 1 - \delta - \mathrm{i}\beta$, where δ is the index of refraction decrement that describes the phase-shifting and dispersion properties of condensed matter and β, the absorption index, describes the absorption properties. These two energy-dependent terms of the index of refraction can be written as $(\delta + \mathrm{i}\beta) = \alpha\lambda^2(f_1 + \mathrm{i}f_2)$, where $\alpha = n_a r_e/2\pi$, with n_a being the number density of atoms, and $r_e = 2.82 \times 10^{-15}$ m is the classical radius of the electron. The corresponding (atomic) photoabsorption cross-section (σ_a) is given by $\sigma_a = 2r_e\lambda f_2$. As an example, Fig. 2 plots the coherent (elastic) scattering cross-section and the photoabsorption cross-section for carbon, the most important element for polymer studies. The graph is based on the atomic scattering factors tabulated by Henke et al. [35] and the NIST XCOM database [37]. These plots clearly show that the cross-sections for absorption and coherent scattering change by many orders of magnitude between the soft X-ray range (<2 keV) and the (conventional) hard X-ray range (>2 keV). The coherent (elastic) scattering cross-section undergoes large changes as a function of photon energies near the characteristic jump of the photoabsorption cross-section associated with absorption edges. The corresponding scattering factors f_1 and f_2, along with those for nitrogen and oxygen, are plotted in Fig. 3 and contrasted to the indices of refraction (δ and β), assuming a density of 1 g/cm^3 for the latter. We note that f_1 and δ also undergo large changes near the respective absorption edges similar to the cross-sections. Furthermore, f_1 is negative right

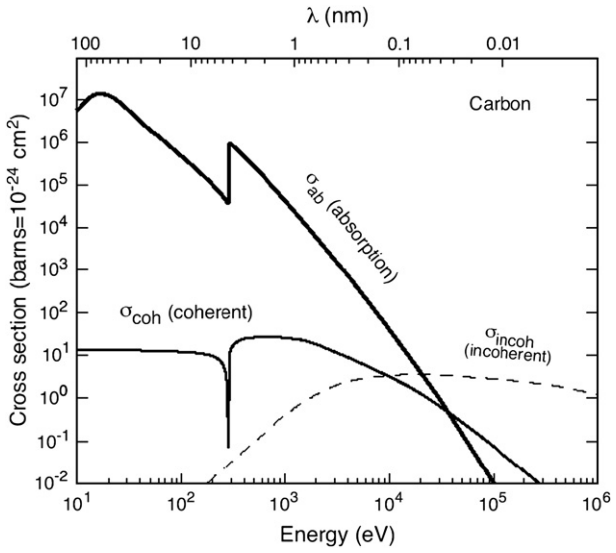

Fig. 2. Cross-sections of X-ray interactions in carbon. At energies below about 10 keV, absorption dominates so that images and scattering experiments are free from the complications of multiple scattering. Data from Henke et al. [35] and the NIST XCOM database [37]. These generalized plots do not take spectral details near absorption edges related to compositional and bonding into account. (Figure courtesy of Jacobsen.)

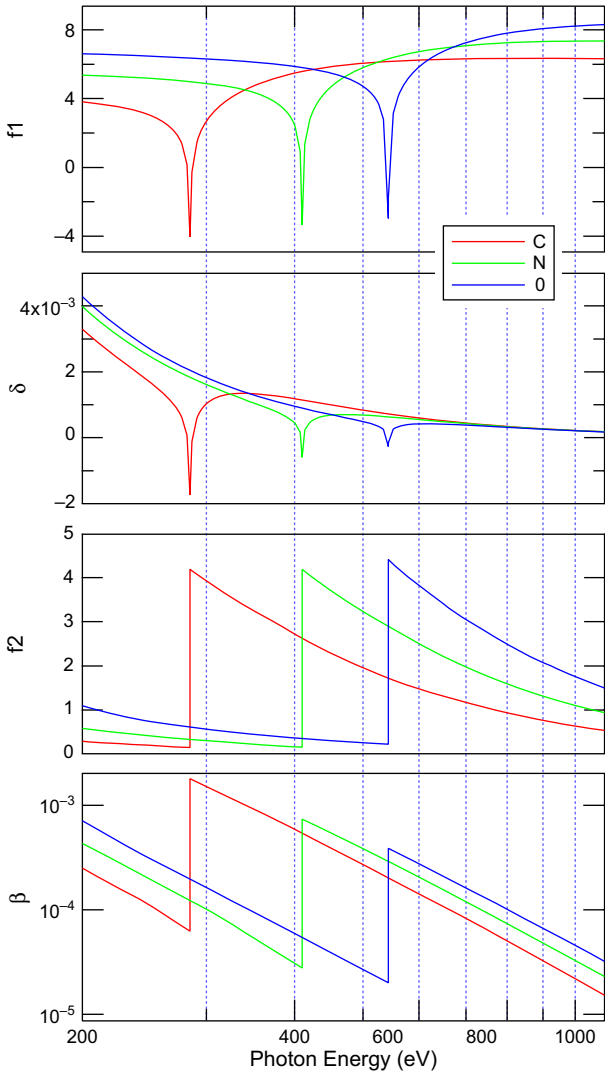

Fig. 3. Energy-dependent scattering factors f_1 and f_2 and the corresponding optical parameters δ and β for carbon, nitrogen, and oxygen, assuming a density of 1 g/cm^3. At X-ray absorption edges (~290 eV for C 1s, ~ 410 eV for N 1s, and ~545 eV for O 1s) f_2 and β have step increments, while f_1 and δ undergo dispersion resonances. Data after Henke et al. [35].

near the edge, but is otherwise relatively constant below the edge and above the edge, i.e. ~4 and ~6 for carbon, respectively. In contrast, δ scales by a factor of λ^2 relative to f_1, which imparts a strong overall energy dependence. However, the scaling does not affect the sign of these variables and δ is negative over the same energy range as f_1. These negative values correspond to an index of refraction for which there is no critical reflection angle ($\theta_c = (2\delta)^{1/2}$). The corresponding behavior can be observed for f_1, f_2, δ, and β for nitrogen and oxygen as well.

In semi-classical models of atoms, these rapid changes in optical properties are modeled by damped forced oscillations, which indeed have a peak in amplitude when the driving frequencies of the photon correspond to the natural frequencies of the atom. It is these resonances that lead to the term ''resonant scattering'', even though the energy range over which this terminology should be applied is not very well defined. The designation ''anomalous'' is derived from the observation of anomalous dispersion of electromagnetic waves that occurs over a well defined energy range near these resonances, determined by the condition $dn/d\lambda > 0$. The terms ''anomalous'' and ''resonant'' are often used as interchangeable, semi-descriptive adjectives. In either Resonant Soft X-ray or conventional (non-resonant) X-ray scattering, the signal detected from a macroscopic sample is the overall diffraction or scattering signal from the heterogeneous sample probed, i.e. the superposition of the waves elastically scattered or perturbed by phase shifts or absorption by all the atoms that are within the coherence volume of the incoming beam. The quantity $\Delta\delta^2 + \Delta\beta^2$, where $\Delta\delta = \delta_2 - \delta_1$ and $\Delta\beta = \beta_2 - \beta_1$ and the indices indicate the two phases, can be considered as a quantitative measure of the scattering or reflectivity contrast between two materials [27]. Conventional (non-resonant) X-ray scattering is only sensitive to phase shifts related to δ. In the resonant (anomalous) region, both the relative dispersive *and* the absorptive properties of matter are important and can be selectively employed by tuning the photon energy. To describe the combined phase-shifting and absorption effect, the use of either ''resonant'' or ''anomalous'' to describe the technique is incorrect in the strictest interpretation of ''resonant'' or ''anomalous''. The necessary inclusion of the effects of absorption requires that the term ''resonant scattering'' be interpreted broadly to mean any rapid and moiety-specific change in $\Delta\delta^2 + \Delta\beta^2$ as a function of photon energy. In the present usage of ''anomalous'' and ''resonant'', the former is more closely associated with hard X-rays [16–19] and the latter with soft X-rays [13–15].

NEXAFS microscopy and RSoXS are naturally complementary techniques. The utility of NEXAFS spectromicroscopy

and RSoXS for studying polymeric materials lies in the fine details of δ and β encountered near the inner shell excitation thresholds. These are highly specific to the molecular structure of the material – functional groups in particular. The following two sections will showcase some of the compositional details in δ and β to be found near absorption edges and delineate their correlation to basic chemical moieties. For additional details of the underlying physics of the interactions of X-rays with matter, the reader is referred to the monograph in Ref. [36] and related literature by Henke et al. [35] and Hubbell et al. [38], as well as the recent comprehensive overview of X-ray microscopy by Howells et al. [34].

2.2. NEXAFS background

NEXAFS is an absorption spectroscopy in which a core electron is excited into empty states near the photo-ionization threshold [20]. It is thus inherently element specific due to the specific elemental binding energies of core electrons. In addition, due to the close relationship between molecular bonding and the structure of the empty electronic states, NEXAFS is very sensitive to the detailed chemical structure of the sample. Fig. 4 presents the C 1s NEXAFS spectra of a number of common polymers, demonstrating the ability of this spectroscopy to differentiate materials on the basis of relatively subtle bonding and structural differences. For instance, saturated structures such as polyethylene (PE) and polypropylene (PP) are readily distinguished from polymers containing C=C bonds, since the latter give rise to intense and narrow C 1s(C=C) → $\pi^*_{C=C}$ peaks around 285 eV. Among the various unsaturated polymers whose spectra are plotted in Fig. 4, those containing both C=C and C=O bonds are readily differentiated from those with solely C=C bonds, due to the occurrence of relatively sharp C 1s(C=O) → $\pi^*_{C=O}$ peaks in the 286–292 eV region. Urquhart and Ade have shown from a study of various molecular solids and polymers that there is a large spread of C 1s(C=O) → $\pi^*_{C=O}$ energies [39], with a good correlation between the excitation energy and the local "oxidation" of the carbonyl. Lessard et al. [40] have made a similar correlation from a study of gas phase carbonyl and dicarbonyl species.

Substituted ring systems, such as *para*-bromopolystyrene (PBrS), are readily distinguished from unsubstituted parent species since there are characteristic shifts of C 1s(C–R) → π^*_{ring} relative to C 1s(C-H) → π^*_{ring} transitions that depend on the charge withdrawing and electronegativity of the R-substituent [41].

For absorption contrast in microscopy, C 1s NEXAFS tends to provide the best signal-to-background (S/B) and signal-to-noise (S/N) acquisition conditions since the C 1s is typically the core level with the lowest energy in most polymers and thus has the highest cross-section and a low background from other electronic excitations and ionizations. Since the electronic structure and bonding of carbon are very diverse, the C 1s edge also offers the best capability to spectrally differentiate chemical species. However, one should remember that there are NEXAFS spectra associated with the core edges of every element in a sample, and in many cases, other edges provide complementary information or even advantages over C 1s NEXAFS. Fig. 5 presents the O 1s NEXAFS spectra

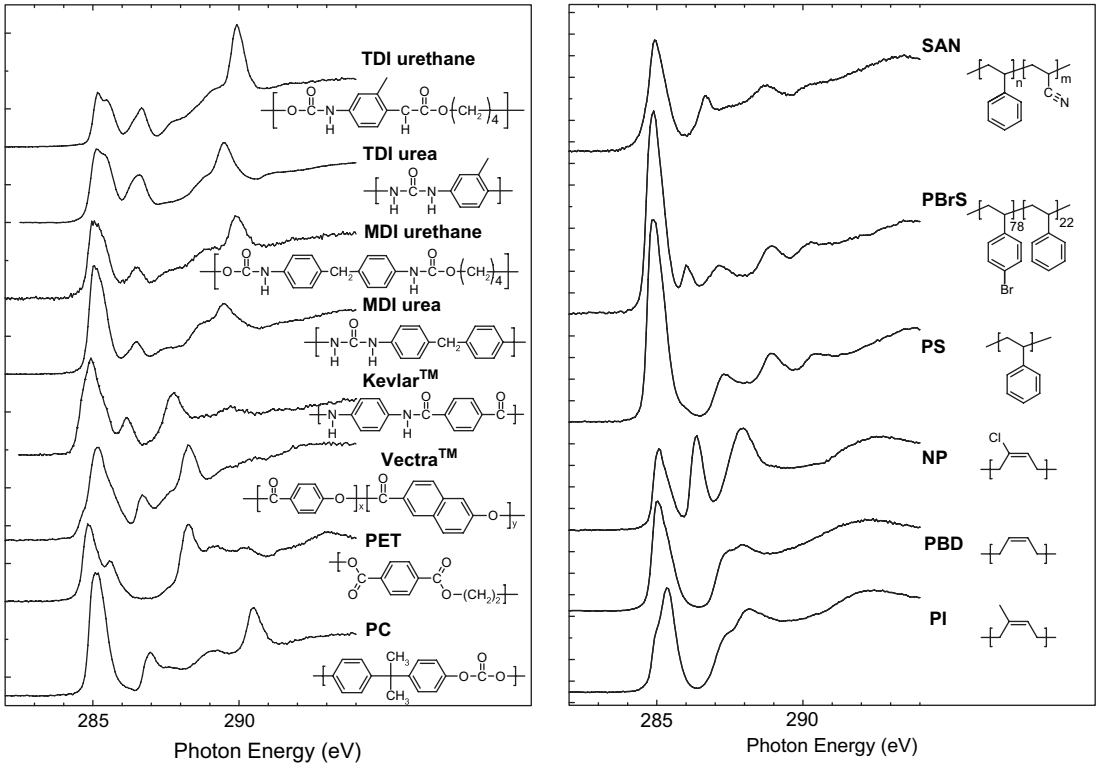

Fig. 4. C 1s NEXAFS spectra of a number of polymers and their chemical structure exemplifying the compositional sensitivity of NEXAFS spectroscopy [32].

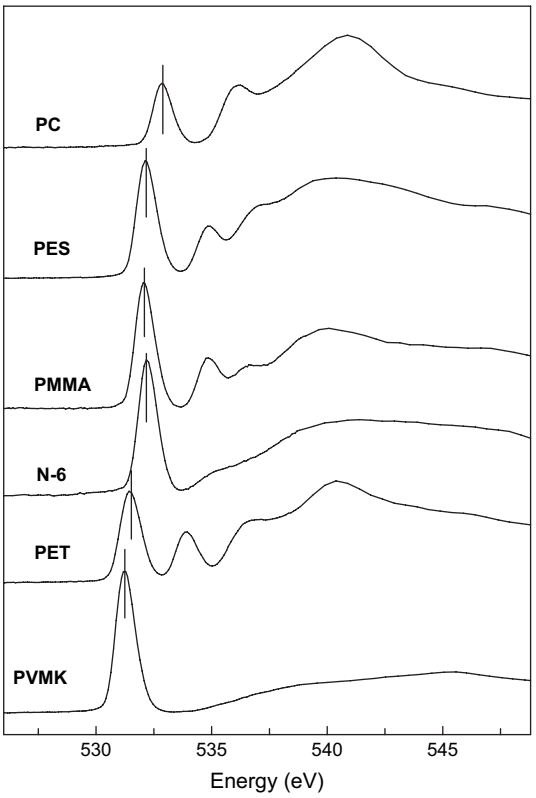

Fig. 5. Examples of O 1s NEXAFS spectra of a number of carbonyl containing polymers [39]: polycarbonate (PC), poly(ethylene succinate) (PES), poly(methyl methacrylate) (PMMA), Nylon-6 (N-6), poly(ethylene terephthalate) (PET), and poly(vinyl methyl ketone) (PVMK).

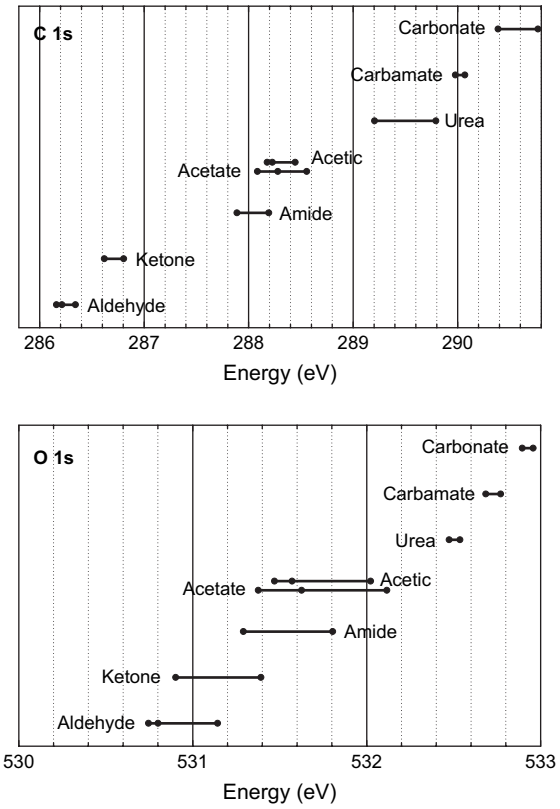

Fig. 6. Spectroscopic correlation diagram for the expected energies of the C 1s(C═O) → $\pi^*_{C=O}$ peaks (top) and the O 1s(C═O) → $\pi^*_{C=O}$ transitions (bottom) in molecules containing the carbonyl group [39].

of a number of polymers to illustrate the spectral features at that edge and their relationships to molecular structure. Analogous to the C 1s edge, unsaturated species in O-NEXAFS are characterized by a sharp low-lying O 1s → π* transition. The range of chemical shifts in these transitions at the oxygen edge is smaller than for the corresponding features at the C 1s edge [39]. Acid and ester groups are readily differentiated from carbonyl or amide groups by the presence of a second O 1s(O–R) → π* transition around 537 eV in the former, which does not exist in the latter.

Phenomenological correlation diagrams similar to IR diagrams can be established [39]. An example that shows the C 1s(C═O) → $\pi^*_{C=O}$ and O 1s(C═O) → $\pi^*_{C=O}$ peak energies of the carbonyl group in different chemical structures is shown in Fig. 6. This trend results in an analytical capability of NEXAFS for the identification of the type of carbonyl functional group that is similar to the C═O stretch frequency in infrared spectroscopy.

In many cases, the spectra of polymers can be understood through the consideration of the spectra of small molecule analogues. A bibliography and databank of inner shell excitation spectra of gaseous small molecules are available (Ref. [42], updates are available from http://unicorn.mcmaster.ca); consultation of that data is often helpful to determine if a given pair of chemical structures is likely to be differentiable by NEXAFS. For small molecules it is also possible to carry out detailed spectral interpretation using a number of different computational packages, such as GSCF3 [43,44], STEX [45], and density functional approaches [46]. Typically, each of these is able to reproduce the main spectral features with correct relative intensities, but with a shift of a few eV from the absolute energy positions. For macromolecules, one typically assumes a 'building block' approach in which the X-ray absorption spectrum of the polymer is similar to that of the repeat unit [20]. The latter can be approximated experimentally by small molecule analogues [47–50] and the interpretation of their spectra can be aided by computation. In polymers with complex and variable repeat units, the building block concept can be applied to estimate (or interpret) the spectrum in terms of an appropriately weighted combination of its constituent parts in cases where these are linked in a way that does not allow significant electronic delocalization (typically at least two saturated bonds between unsaturated structures). Thus the C 1s spectrum of phenylalanine is well reproduced by the sum of the C 1s spectra of benzene and alanine [51]. For analytical purposes, this means that the spectrum of copolymers, such as poly(S-*r*-AN), can be reproduced by the sum of appropriately weighted spectra of polystyrene (PS) and polyacrylonitrile (PAN), giving rise to accurate quantitation of the composition – see Fig. 7. While these simple additive approaches to spectral interpretation are able to explain many spectral features and provide a route to quantitation, there are certainly exceptions where this approach fails, typically on account of electronic delocalization. Even in cases where

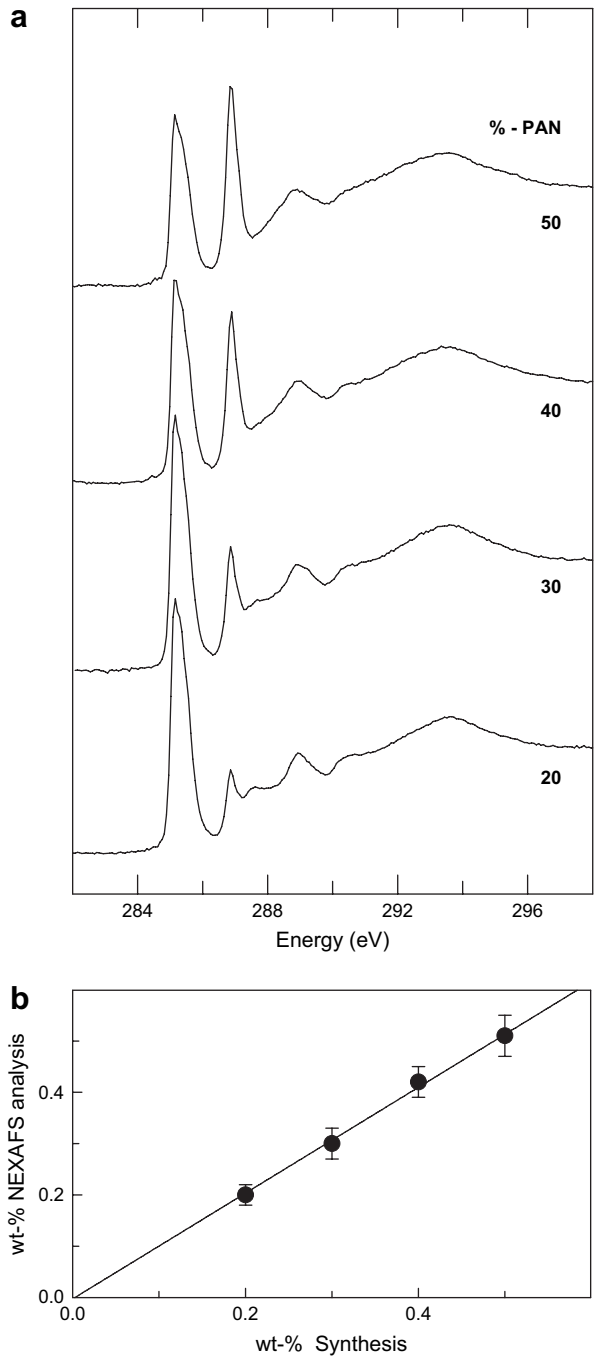

Fig. 7. (a) NEXAFS spectra of four poly(S-*r*-AN) polymers with the nominal wt% AN indicated and (b) wt% AN derived by fitting these spectra to reference standards, plotted against the nominal wt% AN from synthesis. (Data measured with NSLS STXM, samples' courtesy Ed. Rightor, The Dow Chemical Company.)

the building approach works to first order, one can find aspects of the polymer spectra that need refinement or different approaches to explain the spectra in full detail.

In addition to chemical identification and quantitation through NEXAFS spectral features, the use of linearly polarized synchrotron light allows exploitation of linear dichroic signals (NEXAFS transitions are electric dipole transitions) to probe spatial orientation and quality of alignment. This effect has been exploited for many years in non-spatially resolved NEXAFS spectroscopy – indeed the determination of the orientation of small molecules at metal surfaces was the initial attraction of NEXAFS [20]. The first exploitation of linear dichroism as a contrast mechanism in soft X-ray microscopy of polymers was reported in 1993 and 1996 [12,52] shortly after the first NEXAFS microscopy experiments in 1992 [11]. However, the number and range of applications utilizing dichroism were slow to emerge due to a combination of technical and sample limitations. The pace has picked up recently, and a number of applications utilizing dichroism have been performed and are discussed in Section 5.6.

2.3. Scattering/reflectivity background

Reciprocal space methods such as neutron scattering and -reflectivity as well as conventional X-ray scattering and reflectivity primarily make use of phase shifts in the sample, i.e. these methods utilize differences in δ, as absorption, β, plays a very minor role at high photon energies or for neutrons [9]. For RSoXS and RSoXR, the situation is markedly different as the relative absorption differences between materials can completely dominate the scattering contrast. In addition, "bond-specific" contrast can be achieved in a manner similar to NEXAFS microscopy, because δ and β change rapidly as a function of photon energy near absorption edges and the quantity $\Delta\delta^2 + \Delta\beta^2$ determines the contrast between materials and their scattering strength [27]. As an example of chemical

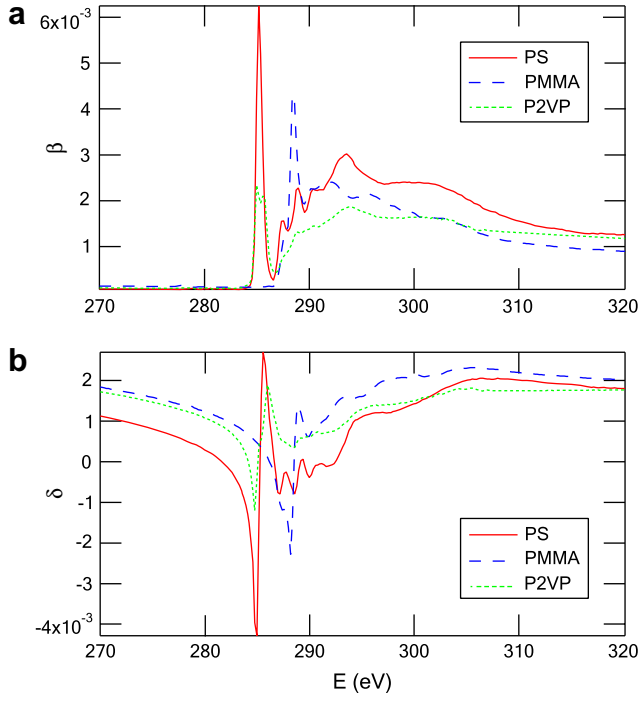

Fig. 8. (a) Absorption β and (b) index of refraction decrement δ for PS, PMMA and P2VP near the carbon K absorption edge. Both δ and β exhibit fine structure near the absorption edge that can be exploited to tune the reflectivity at an interface or the scattering contrast between different phases (see Fig. 9) [27].

specificity, δ and β are displayed in Fig. 8 as a function of energy for polystyrene (PS), poly(methyl methacrylate) (PMMA) and poly(2-vinylpyridine) (P2VP). The contrast, $\Delta\delta^2 + \Delta\beta^2$, for the PS/PMMA, PS/vacuum, and PMMA/vacuum interfaces is shown in Fig. 9a. In addition, $\Delta\delta^2 + \Delta\beta^2$ is shown for the PS/P2VP, P2VP/vacuum, and P2VP/PMMA systems in Fig. 9b, and for PS/PMMA over a larger energy range in Fig. 9c. Clearly, the complex index of refraction and contrast between materials exhibit rapid and specific changes near the absorption edges. As a consequence, the contrast is significantly enhanced at specific photon energies. The structural difference between PS and P2VP is just the replacement of a carbon atom with a nitrogen hetero-atom in an aromatic group, yet the resulting changes of δ and β are rather pronounced. Since δ can be calculated from β through Kramers–Kronig integral relations, the NEXAFS absorption spectra compiled by Dhez et al. and Urquhart and Ade of synthetic polymers [39,53] and Kaznacheyev et al. [54] for biopolymers and Zubavichus et al. for amino acids [55] can serve as a guide to show how powerful and general the relatively novel methods RSoXS and RSoXR might be [27,36]. The scattering contrast can be computed and assessed prior to experiments in order to select energies with the best contrast and information content. The spectral richness of the scattering contrast $\Delta\delta^2 + \Delta\beta^2$ will complement and mirror the spectral richness of β already used extensively in NEXAFS spectroscopy and microscopy of carbonaceous materials [11,20,31,53].

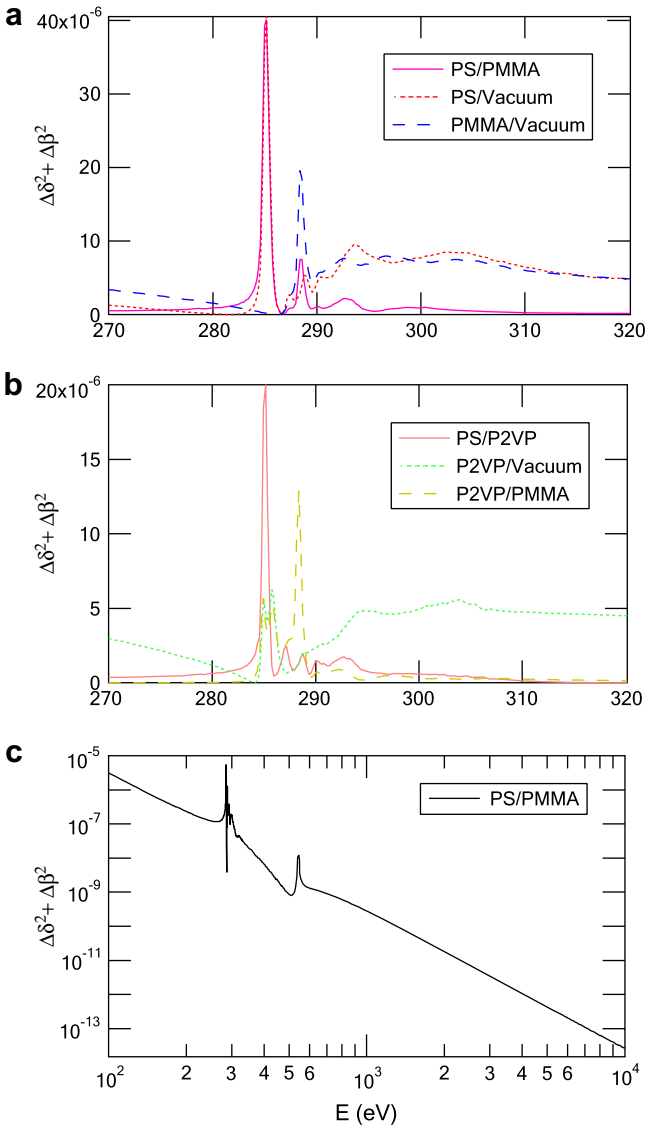

Fig. 9. (a) Materials' contrast and "scattering strength", $\Delta\delta^2 + \Delta\beta^2$, of the PS/PMMA, PS/vacuum, and PMMA/vacuum interfaces near the carbon K-edge. (b) $\Delta\delta^2 + \Delta\beta^2$ of PS/P2VP, P2VP/vacuum, and P2VP/PMMA interface. (c) $\Delta\delta^2 + \Delta\beta^2$ for PS/PMMA over a larger range of photon energies [27]. The feature near the oxygen edge at ~540 eV does not take into account the finer details that one would expect for PMMA. It is solely due to the edge jump based on the absorption data tabulated by Henke et al. [35].

Use of RSoXS and RSoXR as alternatives to conventional methods will be most fruitful for the characterization of multicomponent systems. We exemplify the possibilities and capabilities by considering the extent of the observed Kissing fringes in a multilayer system and their dependence on photon energy. The reflectance in such a system depends on the relative reflectivity at each interface as well as the absorption in each layer. This complex behavior is best illustrated by simulations. The calculated reflectance is shown in Fig. 10 from perfectly sharp layers of 15 nm PS on top of 45 nm PMMA – a thickness ratio of 1:3 – on a silicon substrate shows the photon energy dependence quite clearly [27]. For 320.0 eV and 14.2 keV photons, almost uniform fringes with $\Delta q \approx 0.105\ \mathrm{nm}^{-1}$ and hence $d \approx 2\pi/\Delta q = 60$ nm are observed. These fringes arise from interference of reflected beams from the PS/vacuum and PMMA/Si interfaces and show very limited sensitivity to the polymer/polymer interface, i.e. there is comparatively little intensity reflected at that interface. In contrast, strong interference effects related to the polymer bilayer structure are readily observed as "beats" (i.e. modulations of the fringe amplitude) at photon energies of 285.2 eV and 288.5 eV. The simulation at 285.2 eV has, for

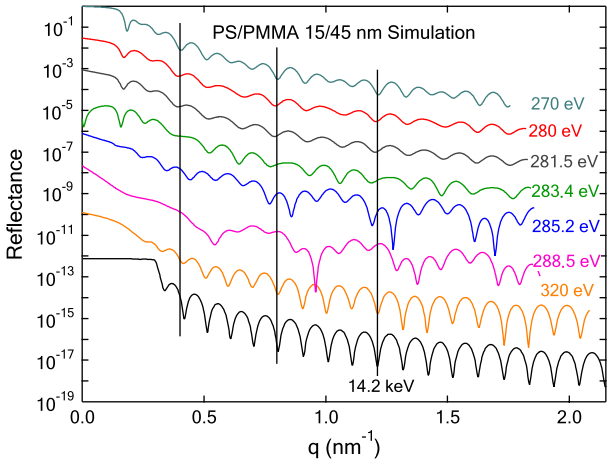

Fig. 10. Calculated reflectivity of a perfectly smooth and sharp 10 nm/30 nm PS/PMMA bilayer at selected photon energies, using the values of δ and β as displayed in Fig. 8. At 14.2 keV and 320 eV, the fringes are dominated by sensitivity to the total film thickness. In contrast to this, 280 eV, 283.4 eV, 285.2 eV, and 288.5 eV show strong sensitivity to the polymer/polymer interface [27].

example, strong beats corresponding to $\Delta q \approx 0.42\ \mathrm{nm}^{-1}$, which is 4 times the Δq that corresponds to the full thickness. This directly implies strong sensitivity to the 15 nm thick PS layer, which is 1/4 of the total film thickness, and the contrast is high due to the large $\Delta\beta^2$. At 270.0 eV, good sensitivity to the PS/PMMA interface is observed, based primarily on $\Delta\delta^2$, although the overall fringe amplitude is reduced compared to 285.2 eV. These simulations demonstrate that careful choice of specific photon energies can greatly improve the sensitivity of RSoXR to a specific interface relative to conventional XR. Similarly, the strong photon energy dependence allows for "bond-specific" scattering in geometries other than specular reflectivity. Experimental results and some of the first applications of these novel soft X-ray tools to the characterization of polymeric materials will be discussed in Section 5.

3. Microscopy background

Even though the capabilities of NEXAFS spectroscopy to achieve compositional analysis as demonstrated in the preceding section are quite high, several spectroscopic methods, such as infrared (IR), nuclear magnetic resonance (NMR), and Raman spectroscopy, have generally higher sensitivity to specific moieties and functional groups. Thus, to be truly useful, NEXAFS microscopy has to exceed the spatial resolution of these complementary spectroscopy techniques. To date, NEXAFS microscopy has achieved a level of spatial resolution at least an order of magnitude better than what can be accomplished with these alternative compositional analysis techniques [21,56]. In addition, NEXAFS microscopy can have high surface sensitivity of about 10 nm through the use of secondary electrons [20]. The surface sensitivity can improve to 0.1–0.3 nm when energy selected photoelectrons are detected in a Photoemission Electron Microscope (PEEM) equipped with an energy analyzer [57–59] or a Scanning Photoemission Electron Microscope (SPEM) [60–63].

High spatial resolution is achieved in two ways: (i) special diffractive optics, generally referred to as Fresnel zone plates, are used in full-field and scanning transmission instruments [33], as well as SPEMs [60,62–64]; and (ii) electron imaging in PEEMs, which allows the characterization of surfaces [56,65]. Zone plate based transmission microscopes are true X-ray microscopes, i.e. photon-in/photon-out, whereas PEEMs are really electron microscopes in which high spatial resolution is achieved with electrostatic or electromagnetic electron optics.

3.1. Transmission X-ray microscope

In a Scanning Transmission X-ray Microscope (STXM), images are obtained by mechanically raster scanning the sample though the focal point of a zone plate X-ray lens (see Fig. 11) [66,67]. In a full-field conventional Transmission X-ray Microscope (TXM), a condenser zone plate upstream of the sample is used to partly monochromatize ($E/\Delta E \sim 100$) and to intensify the X-rays on the sample. This arrangement also closely matches the numerical aperture of the illumination to the numerical aperture of the imaging zone plate that magnifies the X-rays transmitted through the sample onto a 2D detector [68–70]. The Rayleigh resolution of a perfect, non-apodized zone plate is 1.22 times the outermost zone width. Hence, the quality of the zone plate is paramount to the intrinsic resolution capabilities of the STXM and the TXM and is limited by the fabrication technologies available. Zone plates with outermost zone widths between 15 nm and 40 nm are presently in use, providing experimental spatial resolutions in the range of 18–45 nm [21,71–74]. This is about an order of magnitude worse than the wavelength limited, far-field diffraction limit of $\lambda/2$ ($\approx$2 nm for energies near the carbon edge). This difference between actual performance and physical limit is the basis for the expectation and optimism for continued and substantial improvements in spatial resolution in the future as the zone plate fabrication technology continues to improve.

NEXAFS microscopy with good compositional sensitivity in the soft X-ray range requires an energy resolution $E/\Delta E$ of >2000. This is most readily achieved with a grazing incidence grating monochromator upstream of the microscope. Near the carbon edge, the most widely used edge for polymeric materials, a resolving power of 2000–5000 is routinely available [67,75,76]. The present zone plate monochromators used in a TXM have relatively low energy resolution ($\sim$0.8 eV), limiting the utility of TXM for NEXAFS microscopy of polymers.

Unfortunately, zone plates are highly chromatic lenses. This necessitates continual refocusing during the photon

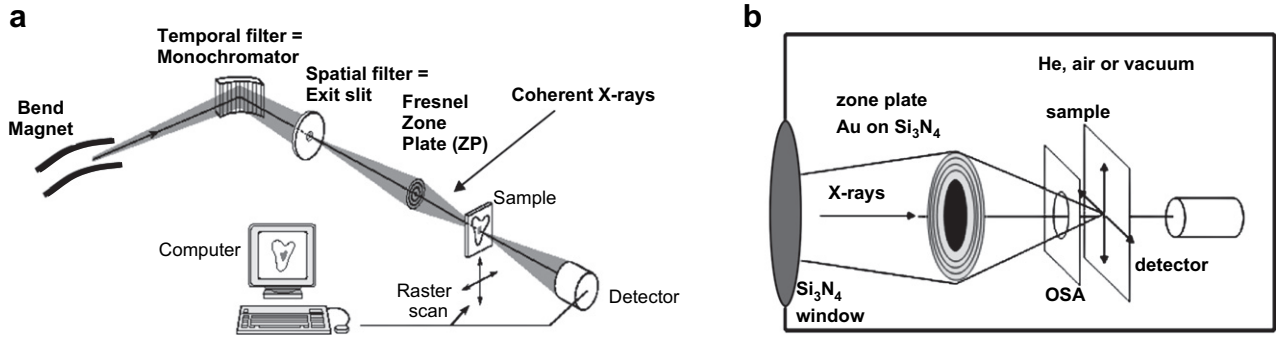

Fig. 11. Schematic of a Scanning Transmission X-ray Microscope (STXM). (a) Source and beamline. (b) Details of the STXM optics.

energy sweep necessary for spectroscopy. The associated and difficult to avoid transverse motion of the sample relative to the optical axis often necessitates post-acquisition compensation during data analysis [77]. The experimental challenges that avoid misalignment of data acquired at different energies have only recently been overcome, in large measure, through the use of laser interferometry [21].

3.2. Photoemission Electron Microscope (PEEM)

To study surfaces with NEXAFS, the sample is flooded with photons and the total photoelectron yield (TEY) or partial electron yield (PEY) signals are measured [20]. These yields track the absorption cross-section as a function of photon energy and provide excellent NEXAFS spectra. PEY traditionally refers to experiments that utilize a bias voltage on the detector or utilize an energy window set with an energy analyzer. Both variants of PEY methods strive to accept only electrons near the minimum of the secondary electron mean free path ($\sim$50 eV to 300 eV kinetic energy) in order to achieve high surface sensitivity of about 1 nm. In a simple PEEM, ''PEY'' detection of a different kind is at work. The photoelectrons emitted from the sample surface are accelerated and imaged onto a two-dimensional detector (Fig. 12). The objective lens in a PEEM in combination with an aperture that is needed to improve spatial resolution acts as a low pass energy filter with a bandwidth of a few eV near the photoelectron threshold. This energy window results in a total sampling depth of about 10 nm [78,79]. A careful measurement of the NEXAFS signal from PEEM studies of different thickness of polystyrene films has determined a critical sampling depth of 4 ± 1 nm [79], consistent with a total sampling depth (integrating out to 98% of the signal) of 10 nm. Use of an energy filter [57–59] allows X-PEEM imaging of selected kinetic energy electrons, and the sampling depth can be reduced considerably to as small as 0.3 nm in some materials [80]. The development of spherical and chromatic aberration compensation optics, pursued in the SMART project at BESSY-II [59] and the PEEM3 project at the Advanced Light Source (ALS) [58], is expected to result in ultrahigh spatial resolution (better than 5 nm). Since PEEMs acquire information in parallel from all pixels in the image, incoherent illumination of the sample is possible and PEEMs can be readily operated at bending magnet beamlines that provide sufficient flux and energy resolution [56,65,81,82]. PEEMs also do not require any refocusing during photon energy changes and the acquisition of NEXAFS spectra is readily accomplished.

3.3. Analysis tools and data acquisition strategies

The most powerful way of using NEXAFS microscopy, although requiring the longest acquisition times, is through acquisition and analysis of a sequence of images acquired at different energies, also called a ''stack'' [77]. The discussion here will emphasize their analysis. The typical goal in NEXAFS microscopy is to identify the chemical species present and to determine their quantitative spatial distribution. In cases where the chemical components and their NEXAFS spectra are known and the samples have uniform thickness, identification can be as simple as examining images recorded at photon energies at which candidate species have strong absorption. In order to confirm identification of any region that is highlighted in this way, one can extract and examine spectra of selected areas, provided enough images at different energies are acquired, using software tools available, either from the original author, Jacobsen [http://xray1.physics.sunysb.edu/], or as part of the aXis2000 package [83].

Fig. 13 illustrates the principle of how individual images in an image sequence can experience great changes in contrast that reflect the composition and morphology overall and the mass thickness of particular components. The transmission images shown are of a simple, binary PS and PMMA thin film blend, annealed on a SiO_x substrate, and subsequently transferred to TEM microscopy grids for STXM characterization. Reference spectra of PS and PMMA are shown, along with the images that correspond to specific energies, as

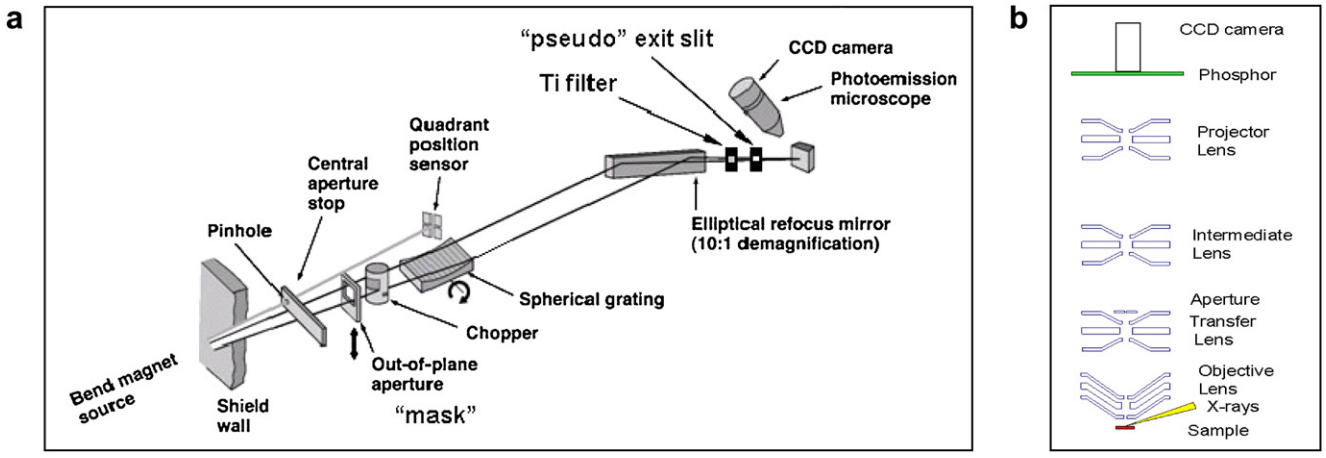

Fig. 12. Schematic of (a) Advanced Light Source beamline 7.3.1 and (b) the Advanced Light Source Photoemission Electron Microscope PEEM2. (Figure courtesy of Andreas Scholl, ALS, LBNL.)

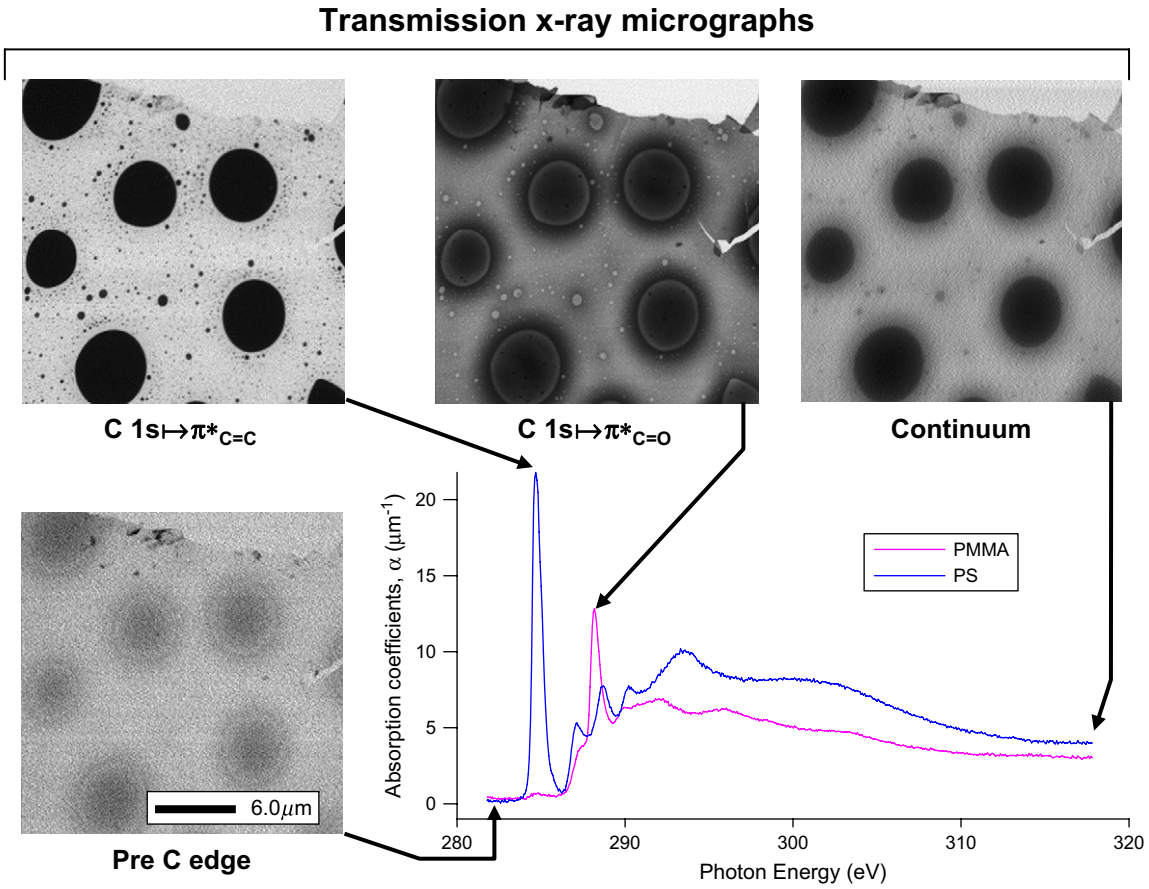

Fig. 13. Transmission images of a simple, binary PS and PMMA thin film blend, annealed on a SiO_x substrate such that large droplets have formed. Reference spectra of PS and PMMA are shown, along with the images that correspond to the characteristic energies as indicated. The complete morphology cannot be inferred from an individual image.

indicated. Even though this should be a relatively simple situation, i.e. two phases of pure homopolymer, any individual image contains only part of the information and is not directly interpretable. The image corresponding to the C 1s(C═C) → $\pi^*_{C=C}$ transition clearly shows the morphology of the PS domains, but it does not indicate by how much the PS is surrounded by PMMA, and any thickness changes associated with the sample. Other energies do not show the morphology of the PS domains clearly, but indicate that the sample is not uniform in thickness. Only the combined information of the images and a more complete and quantitative analysis using a singular value decomposition (SVD) process yield an interpretable model of the sample (see below) [84].

In general, analysis of image sequences in NEXAFS microscopy is an example of an highly over-determined, but poorly conditioned inversion problem. A typical sequence might involve images with 100×100 or 10^4 pixels, recorded at 100 photon energies. If a principle component analysis is performed one might find that there are at most five statistically significant chemical components. If one knows the species present and their NEXAFS spectra, then chemical component maps – the quantitative spatial distribution of each species – can be derived by matching the spectrum at each pixel to a linear combination of the reference spectra. In some cases reference spectra can be extracted from the image sequence itself, if there are areas of pure material. In most cases, this is not possible, and thus the spectra of pure materials must be recorded separately, ideally with the same instrument. The quantitative component maps can be derived using conventional least-squares curve fitting procedures or by singular value decomposition (SVD) [85,86], which is an optimized matrix method to invert data of this type. There is in general no exact solution to the inversion from measured data to component maps in the case of over-determined systems. The optimum solution is a ''close'' result that satisfies in some sense all equations simultaneously. This closeness can be defined in a least-squares sense and may be calculated by minimizing the residual error [86]. An illustration of the procedure and outcome is shown in Fig. 14. An interpretable model of the PS/PMMA thin film as shown in Fig. 13 emerges when using the SVD procedure and the results clearly show large and thick PS droplets surrounded by a sloping rim of PMMA in such a way that the total film thickness changes smoothly in height. During annealing on the substrate, PS droplets form that cannot sink into the PMMA matrix as the film is too thin. This thin film constraint and the balancing of interfacial energies force the contact line between PS and PMMA to be relatively high on the PS droplets, leading to

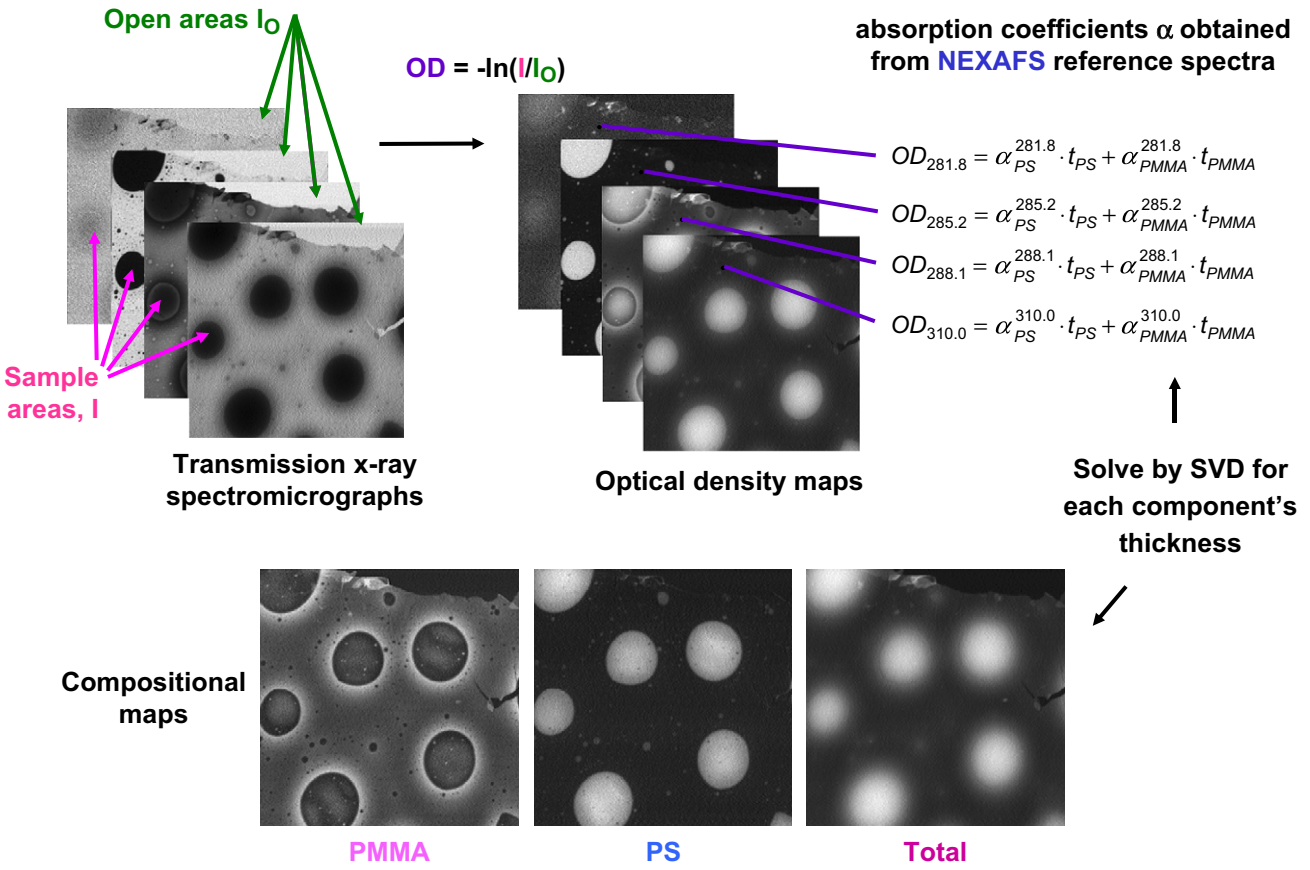

Fig. 14. Principles of singular value decomposition (SVD). The transmission images are converted to optical density and a matrix transform that uses knowledge about the linear absorption coefficients yields quantitative mass-thickness maps. The morphology and related thickness variations of the sample are interpretable only after the SVD procedure.

a ''rim'' of PMMA that surrounds the PS droplets. Additional subtleties of the morphology in these thin films could be interpreted due to the quantitative information gained from the SVD procedure [84].

In the case of STXM, where the detected signal expressed as an optical density (OD) is quantitatively related to amount, the reference spectra should be prepared on a linear absorbance scale (OD per nm of material). In situations such as PEEM, where the measured intensities are only indirectly related to amounts, or if one does not convert reference spectra to an absolute intensity scale, one can still apply these methods, but the component maps will only give information about spatial distributions, and at best, relative amounts. If one can measure [79] or estimate the sampling depth for a given system, and is comfortable assuming a similar work function for different regions of a surface, then in some circumstances a quantitative analysis can be performed. An example of this is the quantitative determination of the distribution of proteins adsorbed on a phase segregated PS/PMMA blend surface [78], for which some results are presented in Section 5.5.

SVD analysis was first applied to STXM data sets by Zhang et al. to quantitatively map DNA/protein ratios in sperm [87]. It has been applied subsequently to measure quantitative distributions in many systems, including multicomponent polymer blend thin films [65,84,88–90], environmental samples [91–93], biomaterials [94], and nanomaterials [95]. An extension to the SVD procedure is often useful in cases where there may be some uncertainty about the absolute OD scales of the image sequence or one or more of the reference spectra. This can come about if only the shape and not the absolute intensity of the incident flux (I_o) is used in deriving OD scales. In such cases, scale errors in I_o are equivalent to constant offsets in OD. Thus a ''stack fit'' routine is available in aXis2000 that automatically adds a constant term to the SVD analysis to compensate [83].

PEEM data require careful analysis as several contrast mechanisms are present simultaneously: (i) composition, i.e. the cross-section difference between different materials at a given photon energy, (ii) topography and (iii) illumination effects. Typically, one is interested primarily in the compositional information and analysis procedures have been developed to disentangle the spectroscopic, i.e. compositional information, from topography and illumination effects. Generally, these methods use pre- and post-edge normalizations of the NEXAFS spectra acquired with PEEM and reference spectra acquired with the same instrument (see for example Morin et al. [96]). The point spread function of a PEEM also has long tails, which can greatly complicate or even prevent quantitative analysis. Different PEEM instruments differ considerably in this regard. Despite the challenges, fully quantitative

analysis of polymer thin film compositions has been derived recently from PEEM data [78]. The approach involves use of reference spectra on linear absorbance scales, and normalization of the sum of the relative thicknesses of each component to the total sampling depth in the material as measured by PEEM [79]. Since work functions and electron propagation are quite material dependent, this is unlikely to be a general technique but will provide semi-quantitative compositional information in cases where all components are chemically similar.

An additional type of information that NEXAFS microscopy provides is molecular orientation, through the linear dichroism aspect of the spectroscopy [12,52]. It is possible to measure images or image sequences at a range of angles that can then be manipulated into a stack in which the control variable is the angle between a reference direction of the sample (e.g. a fiber axis) and the X-ray E-vector. Routines to fit such angle-dependent image sequences are available in aXis2000. They provide maps of the director – the local orientation angle – as well as the amplitudes of the dichroic and non-dichroic components [97]. These procedures have been used to study crystallite distributions in cocoon silk [98], dragline spider silks [99] and liquid crystal thin films [100]. Further discussion and examples are provided in Section 5.6.

3.4. Sample requirements

For NEXAFS transmission microscopy near the carbon edge, a sample thickness between 50 nm and 200 nm provides an optimum signal-to-noise ratio, while avoiding spectral distortion due to absorption saturation. Ultramicrotomy or cryomicrotomy or other methods adopted from the TEM community are often employed for bulk materials to prepare samples that meet these requirements. Thin films can also be spun-cast to the right thickness and transferred via the surfaces of suitable liquids to TEM grids or Si_3N_4 windows for X-ray microscopic inspection. Thin samples and section of samples can also be examined in a completely hydrated/solvated state by sandwiching the material and liquid between two very thin Si_3N_4 membranes [101,102]. A design for a robust wet cell that allows fluid transfer and is vacuum compatible has been published recently [103]. For surface analysis in a PEEM, polymer thin films need to have a thickness of less than ~150 nm and be prepared on a conducting substrate. Precise temperature control in STXM and TXM is not yet routinely available. PE samples have been melted near 120 °C [104], biological materials have been examined in the frozen state [105], and phase-change microcapsules have been investigated [106]. Temperatures in a PEEM can range from −70 °C to >1200 °C, with limited accuracy near room temperatures.

3.5. Radiation damage – monitoring, mitigating and exploiting

X-rays provide 100–1000 times as much spectral analytical informations per unit dose than EELS [107], basically because most inelastic electron scattering events excite valence electrons, which do not give NEXAFS equivalent analytical information. Whereas there is an intrinsic advantage, it is also true that the doses of soft X-rays typically used in all types of soft X-ray microscopes have great capability to modify polymers through various radiation damage mechanisms. Thus it is critical that the extent of damage be carefully monitored and that steps be taken to limit the dose to a level that does not compromise the analysis. In terms of the dose required, the hierarchy of radiation induced modifications includes: (i) incapacitation of biological function; (ii) organizational changes – affecting inter-molecular organization and orientation; (iii) chemical transformation – bond breaking, formation, and reorganization; and (iv) mass loss. The loss of biological function is of course just a very sensitive ''detector'' of organizational changes or chemical transformation. Organizational changes can be monitored by changes in the NEXAFS dichroic signal [98] or the elastic scattering signal. Chemical modification is typically readily monitored at a specific photon energy associated with the bond being removed or introduced [79,108–111]. It is a good STXM practice to image at such an energy over a larger field of view of the sample after any analytical image, line scan spectrum or image sequence in order to detect radiation damage. Instrumental measures adopted to limit the dose as much as possible include: (i) piezo-driven in-vacuum shutters [21] which block the X-ray beam in much less than 1 ms, and are used between each line and sometime each point, (ii) defocusing (where appropriate); and (iii) use of image sequences rather than point or line scans, since the effective exposure per pixel can be much smaller for equivalent spectral quality in image sequences due to technical limitations in point spectra or line scan mode or the use of averaging of spectrally equivalent pixels in image stacks.

Whereas radiation modification of samples is generally an undesirable aspect of soft X-ray spectromicroscopy of polymers, the fine focus in STXM, combined with spectral differentiation, and a novel sample structure have recently been used to develop techniques for chemically selective patterning of polymer composites [111]. While aspects of the radiation damage process are currently limiting the effective pattern resolution to ~100 nm, further improvements of the technique may result in a useful lithographic procedure with novel applications.

4. RSoXS and RSoXR experimental requirements

The experimental methods and principles used for RSoXS and RSoXR are similar to conventional X-ray scattering/reflectivity. A collimated X-ray beam is directed at the sample that is mounted on a goniometer. Due to the much longer wavelength used in RSoXS/RSoXR, the scattering angles tend to be much larger for soft X-rays than for hard X-rays. These large scattering angles make it easy to achieve high q-resolution [27]. However, RSoXS and RSoXR require the use of tunable, low energy photons, which in turn necessitates the use of a synchrotron radiation source and a gracing incidence monochromator and beamline. RSoXS and RSoXR

are thus techniques that will not be able to be implemented in a laboratory setting given present laboratory source capabilities. A typical RSoXS/RSoXR arrangement can be found at beamline 6.3.2 at the ALS in Berkeley [112], in which the X-rays are detected in an s-polarization geometry. Although orientation in the sample would affect the optical constants near absorption edges and hence the contrast, the optical properties remain constant during all possible scattering scans in s-polarization and the data analysis would not be unduly complicated by orientation. The down side of the s-polarization geometry is that orientation in samples cannot be readily and explicitly probed. Switching between s- and p-scattering would be a strategy to investigate orientation, but this has not been demonstrated so far. Compared to the X-ray microscopic methods described above, the instrumentation of RSoXS and RSoXR is relatively simple and uncomplicated. This will make it easy for new users to use these methods. On account of the relative simplicity of the RSoXS/RSoXR instrumentation and the familiarity of the macromolecular community with scattering methods, we refer the reader to the literature for details of RSoXS/RSoXR instrumentation [112].

The sample requirements for RSoXS or RSoXR experiments are comparable to NEXAFS microscopy. Either thin films on substrates [13,27] or thin film samples supported on Si_3N_4 membranes [14,15] are utilized. The suitability of using ultramicrotomed thin films has not yet been investigated. The beam size at ALS beamline 6.3.2 is about 150 μm × 15 μm and is never spread out too much on the sample due to the large sample and detector angles. Thus the sample can be quite small in comparison to conventional X-ray and neutron scattering. Typical samples for RSoXS/RSoXR are just a few mm in size and in transmission can be only a little larger than the beam size.

Radiation damage is generally not a problem for RSoXS and RSoXR. In fact, it is one of the key advantages of scattering that the radiation dose is distributed over a large number of structures. The ‘‘cost’’ of this advantage is that only ensemble averaged spatial information is obtained.

5. Microscopy applications

NEXAFS microscopy provides unique or correlative capabilities to characterize organic materials [11,113–116] and has been successfully applied in a wide range of fields, including polymer science, biology, environmental science, interplanetary dust particles, etc. The following discussion will focus on the characterization of synthetic macromolecules and will exemplify the capabilities of NEXAFS microscopy through a number of case studies that are representative for classes of materials. A somewhat terse complement is provided in Appendix A that provides an overview of the applications not discussed here. These two sections when considered together provide a comprehensive review of the field. Additional details on some of the earlier experiments can be found in summary form in previous reviews [31,50,113–115,117,118]. A bibliography of publications on soft X-ray microscopy, with coded identification of those dealing with polymers is available as Supplementary material, and from http://unicorn.mcmaster.ca.

5.1. Polyurethanes and other multicomponent materials

Polyurethane (PUR) based materials either in their neat form or with reinforcing particles are very heterogeneous materials with multiple phases whose compositions are not well known. In many ways, these are some of the most challenging materials to characterize as the complex chemical reactions during production of these materials lead to phase separation over a range of length scales (nanometer to micron) as well as to a number of chemical moieties, some of which are difficult to quantify even with excellent bulk average characterization methods such as IR. It is generally believed that details of the segregated structure determine the versatile and excellent properties of PUR materials and their wide range of applications. The composition/morphology can vary substantially based on formulation chemistry and can be further manipulated through control of processing parameters such as pressure and temperature. The relationship of morphology to material properties is thus an important aspect that needs to be better understood. TEM and SPM can visualize some of the morphologies present and SPM can even determine the distribution of elastic properties, but neither method can provide compositional information. Any detailed compositional characterization with EELS is impossible, as PUR based materials are very radiation sensitive. Characterization methods such as IR and Raman imaging fail, as important morphological details of PUR materials are often at a length scale below the resolution limits of IR and Raman microscopy. Thus, PUR are materials where the combination of relatively high spatial resolution, compositional sensitivity, and relatively low radiation damage of NEXAFS microscopy results in unique contributions to the characterization and understanding of these materials. A number of studies of the spectroscopy of relevant materials and compounds have been performed to provide the required background information [50,119]. Subsequently a number of polyurethane materials have been characterized [50,94,116,120]. The comprehensive study by Rightor et al. [120] resulted in the quantitative analysis of microphase-separated domains and the surrounding matrix materials. An NEXAFS image that clearly delineates macrophase-separated domains is shown in Fig. 15, along with the average NEXAFS spectra of these domains and the surrounding matrix. Although there was a large body of indirect evidence indicating that the observed macrophase segregated features in water rich polyurethane foams are due principally to urea components, the work by Rightor et al. provided the first direct, spatially resolved spectroscopic proof. Thus NEXAFS microscopy could unambiguously resolve the long standing question of the composition of these microphase-separated domains in high water content PUR materials. Furthermore, these urea-rich domains exhibited surprisingly diffusive interfaces that contrasted with the sharp delineation of the ‘urea-balls’ as envisioned prior to the study by

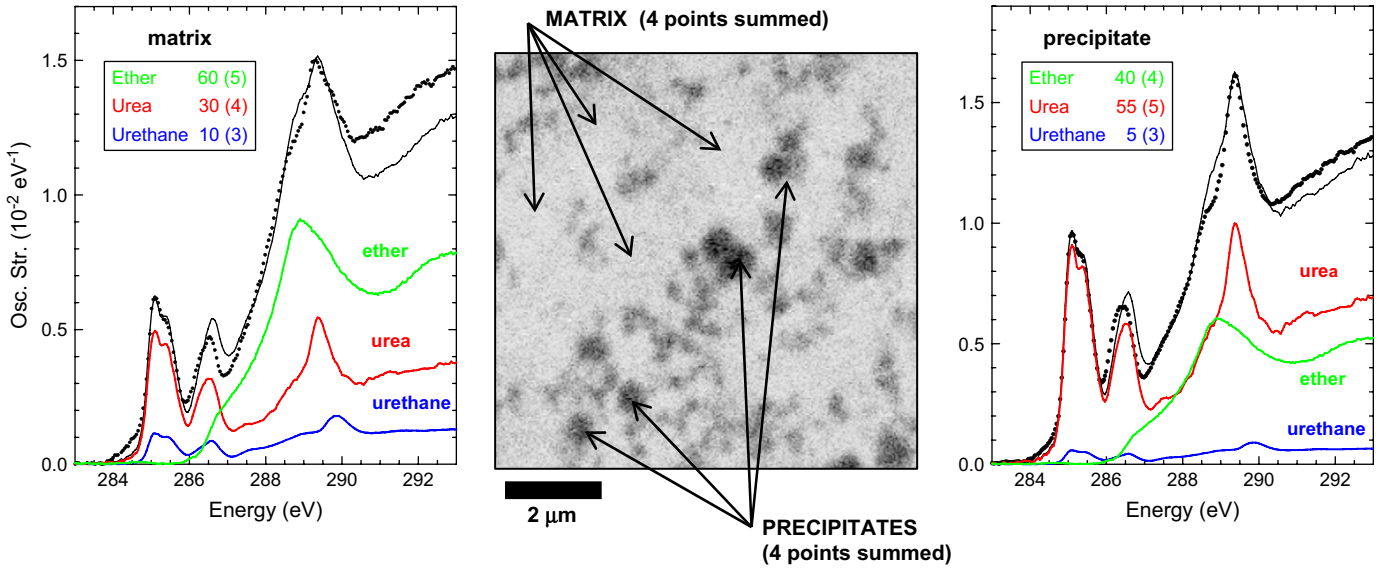

Fig. 15. (Center) Transmission image at 285.2 eV of a butylene oxide-based polyurethane and point spectra acquired with a fully focused beam (~50 nm) at locations indicated by the arrows. The average of four matrix spectra is plotted as the data points in the left hand graph which also includes a fit to a linear combination of the NEXAFS spectra of reference components. The analogous presentation for the average of the four precipitate spectra is shown on the right. The quantitative compositions (urea, urethane and polyol functionalities) of the matrix and the precipitates could be deduced (adapted from Ref. [120]).

Rightor et al. Detailed chemical maps of the urea, urethane and polyether distributions also showed the urea-rich segregated phases to be chemically diffused in a butylene oxide-based foam and to be present as a partial network in an ethylene oxide/propylene oxide-based material [120], further elucidating differences in morphology related to formulation chemistry and ultimately to the corresponding material properties.

Numerous other multicomponent polymer systems have been successfully investigated with NEXAFS microscopy in situations where other tools lacked sensitivity or the required spatial resolution. For example, the efficacy of mechanical alloying and related methods was evaluated with NEXAFS microscopy for a number of polymer systems for which staining and TEM characterization are not an option [121–127]. Materials investigated include blends of poly(ethylene-*alt*-propylene) (PEP), polyisoprene (PI) and PMMA [121,124–126,128]. Even though PI can be readily differentiated from PMMA with TEM by heavy metal staining of PI, PEP and PMMA cannot be easily differentiated. NEXAFS microscopy made visible the intimate mixing at the nanoscale that was achieved. NEXAFS microscopy also helped elucidate directly an unexpected outcome in the PMMA/PEP system. Consolidation at temperatures above the glass transition temperature of PMMA of the cryo-milled powders produced by short milling times resulted in dispersions of PEP in 75/25 w/w PMMA/PEP blends. As the milling time increased to 10 h, however, the consistency of the blends changed from rigid to pliable. NEXAFS microscopy revealed that PMMA becomes the dispersed phase upon consolidation after long milling times. This directly showed that a phase inversion occurred during consolidation after cryo-milling [126], which is the underlying cause of the change in the mechanical properties.

Additional applications of NEXAFS microscopy to composites and blends are detailed in Appendix A.

5.2. Polymer encapsulation structures: microspheres/microcapsules/tectocapsules

Capsules and core–shell microspheres are being used for controlled chemical release in applications such as adhesives, the delivery of agricultural chemicals such as pheromones for biological based agricultural pest control, drug delivery, etc. Novel multi-layered shell structures self-assembled from polymer blends and grafts are being developed as potential optical devices [129]. The properties of these systems – compatibility, release rate, resistance to a specific environment – are optimized for a given application by tuning the porosity and chemistry of the spatially differentiated components of the system. STXM has been used to assist optimization of a number of such systems, including core–shell microspheres [130,131], onion-like particles [129], polyurea [132], alginate capsules [133], and to investigate the structure and radiation stability of phase-change core–shell microcapsules which are used for thermal stabilization of buildings [106].

An example of the 'value-added' by NEXAFS microscopy is the optimization of polyurea capsules [132]. STXM was able to show the relationship of monomer components and quality of the chemical gradient achieved in a sub-micron thick wall. This in turn has lead to information about competing mechanisms of wall formation which has provided general guidelines for optimizing chemical gradients across the walls of capsules which can then be used to tailor the properties for specific controlled release applications. Two other examples – core–shell microspheres and tectocapsules – are discussed in greater detail below, in part to illustrate details of the analysis of NEXAFS microscopic data, and to indicate the additional insights provided.

An early STXM study of the composition of ~0.5 μm sized shells in EGDMA-DVB55 core–shell polymer

structures was reported by Koprinarov et al. [131]. This system has been recently re-investigated. Due to significant improvements of the current generation of STXM over that first developed at the ALS, the images and thus the analysis are of much higher quality. The results for the shell analysis are in excellent agreement with that expected from the synthetic procedure and analysis of the reacting system. Quantitative results from analysis of the STXM C 1s image sequence for one of these core–shell microsphere samples are presented in Fig. 16. Fig. 16a plots the reference spectra on an absolute linear scale in μm^{-1}, established by matching to the indicated absorption curves for the elemental compositions. These spectra were used in an SVD analysis of the C 1s image sequence to derive spatial distributions, called component maps, which are

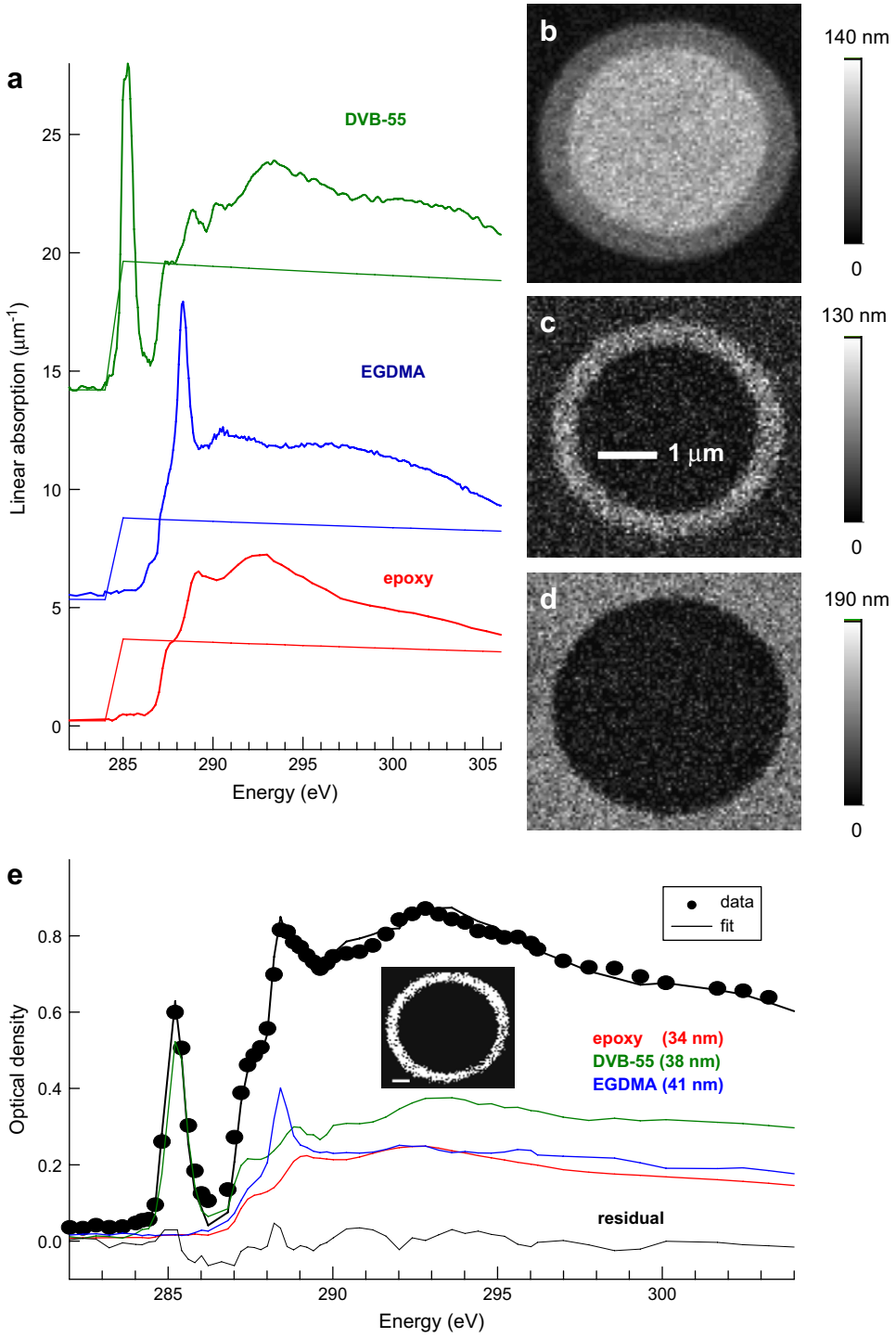

Fig. 16. (a) Reference spectra of the epoxy, DVB55 and EGDMA on absolute linear absorbance scale, established by matching to the elemental response curves (thin lines). (b–d) Quantitative component maps (gray scale thickness in nm) of DVB55, EGDMA and epoxy. (e) Curve fit analysis of the spectrum extracted from the shell region (mask is indicated in the inset). The thicknesses of each component is indicated in nm.

displayed in Fig. 16b–d. Note that the gray scale of each component map is a quantitative measure of the sample thickness (in nm) at each pixel of the map. As with any data analysis, it is important to examine the quality of the result. One measure is the residuals of the fit in both spectral and spatial domains. A second approach is to apply threshold masking to the component maps to extract spectra from a particular spatial region in order to explore the quality of the curve fit. This is illustrated for the critical shell region in Fig. 16e. Clearly in this case the fit is of very good quality so that one can have considerable confidence that the shell was indeed a 50:50 mixture of DVB55 and EDGMA in this sample. In general, it is very prudent to check on every NEXAFS microscopic analysis by examining the quality of the spectral fit in specific regions, such as the shell region in this sample.

Recently Jacobsen has provided a useful tool for analysis of image sequences [134], using sophisticated multivariate statistical analysis (MSA) techniques [85,135] similar to those used in related fields. The merit of this approach is that it provides a means to perform a 'standard-less' analysis which effectively uses the highly redundant nature of the spectral domain information. Typically, a STXM image sequence consists of 10^4–10^5 spectra, for systems in which it is statistically meaningful to identify only 5–7 components. The procedure (PCA_GUI – available at http://xray1.physics.sunysb.edu/) first performs a principle component (PC) analysis which identifies power weighted eigenspectra and associated eigenimages. The user then selects an appropriate number of PCs to further process the data with a cluster analysis, which is a procedure to find a means of combining the PCs in such a way that they group together into clusters in ''PC-space''. These cluster spectra are typically much closer to true NEXAFS spectra of chemical components, although it is not always true that the cluster approach gives correct spectral and thus chemical identification. Fig. 17 presents results from analysis of the same C 1s image sequence of the core–shell microsphere with a 50:50 DVB55–EGDMA shell for which the SVD analysis is presented in Fig. 16. In this case the PC analysis clearly indicated that only three components were present. The cluster spectra derived from the target analysis are displayed in Fig. 17a, while three cuts through the PC-space (C1 vs C2, C1 vs C3, and C2 vs C3) are displayed in Fig. 17b. The latter presentation shows that the target analysis (Euclidian metric) produces a very clean grouping of the data into three spectra, and that the resulting spectra are very plausible NEXAFS spectra. That for component 1 is identically that of the epoxy resin and that for component 2 is identically that of DVB55 in the core. Unfortunately component 3 is the spectrum of the shell, which is known from the material synthesis to be a composite of DVB55 and EGDMA. Thus when these cluster spectra are used to fit the data, the result is simply a separation into three spatial components (Fig. 17c), without a clear indication that the shell is a mixture of two chemical species. PCA_GUI does provide a target analysis procedure in which it is possible to introduce reference spectra of chemical components that are known to be present. When the spectrum of EGDMA is used instead of component 3, the result (Fig. 17d) is virtually the same as that from SVD. In our view both SVD and MSA (as implemented in PCA_GUI) approaches are valuable tools. The limitation of both approaches is that they always give an answer. It is essential that the analyst probes these answers to verify that they indeed represent the chemistry of the sample.

Recently two different encapsulation technologies – microspheres and capsules have been combined in an assembled composite or 'tectocapsule' [130,136]. In this novel approach to controlled release, the barrier functionality is provided by the capsule chemistry, while the release functionality is provided by the properties of porous microspheres embedded in an otherwise impermeable capsule wall. The polyurea capsules are generated through interfacial polymerization in an emulsion. The microspheres are prepared separately by single or multi-step precipitation polymerization and are added to the capsule synthesis system. Initial attempts to combine microspheres and capsules failed as the microspheres prefer the hydrophobic environment of the interior of the capsule. Use of a maleic anhydride-based acid linker greatly improved the microstructure, with the microspheres penetrating the capsule wall but sitting mostly on the outside of it [130,136]. STXM was used to explore the spatial distribution of the acid linker, and thus to optimize its efficiency at controlling the assembly. Fig. 18a and b are SEM images of a tectocapsule, while Fig. 18c is a color coded chemical map derived from a C 1s STXM image sequence. The DVB55 microsphere signal (red), the polyurea capsule signal (green) and the acid linker signal (blue) have been combined to show the overall structure. The chemical map of the acid linker (Fig. 18d) used to control the attachment of the microsphere to the outer surface of the polyurea capsule shows that the acid linker (compatibilizer) is very much concentrated at the outer rim of the microspheres, with an amount that is a few percent of the material in the rim region of the microsphere, but that is extremely low when averaged over the whole tectocapsule.

5.3. Super absorbent polymers and microgels

In addition to investigations of thin sections or thin films of organic materials in the ''dry state'', NEXAFS microscopy has the capability to investigate fully hydrated or solvated materials. In this operating mode, samples are typically sandwiched between two thin Si_3N_4 membranes, which are typically 75 nm or 100 nm thick. Depending on the sophistication required, these so-called ''wet cells'' are either sealed or can have connections for continuous fluid flow [103]. The wet-cell capability has been used to map the cross-link density in a super adsorbent polymer (SAP) [102], characterize the size and charge state in microgels [137], and a number of environmental studies that involve solvated biopolymer such as various polysaccharides and proteins. The generally applicable advantages of NEXAFS microscopy have been extended to the wet state.

Surface cross-linked SAP is highly engineered third generation absorbent material with a wide range of applications. These materials are used in baby diapers, other hygiene

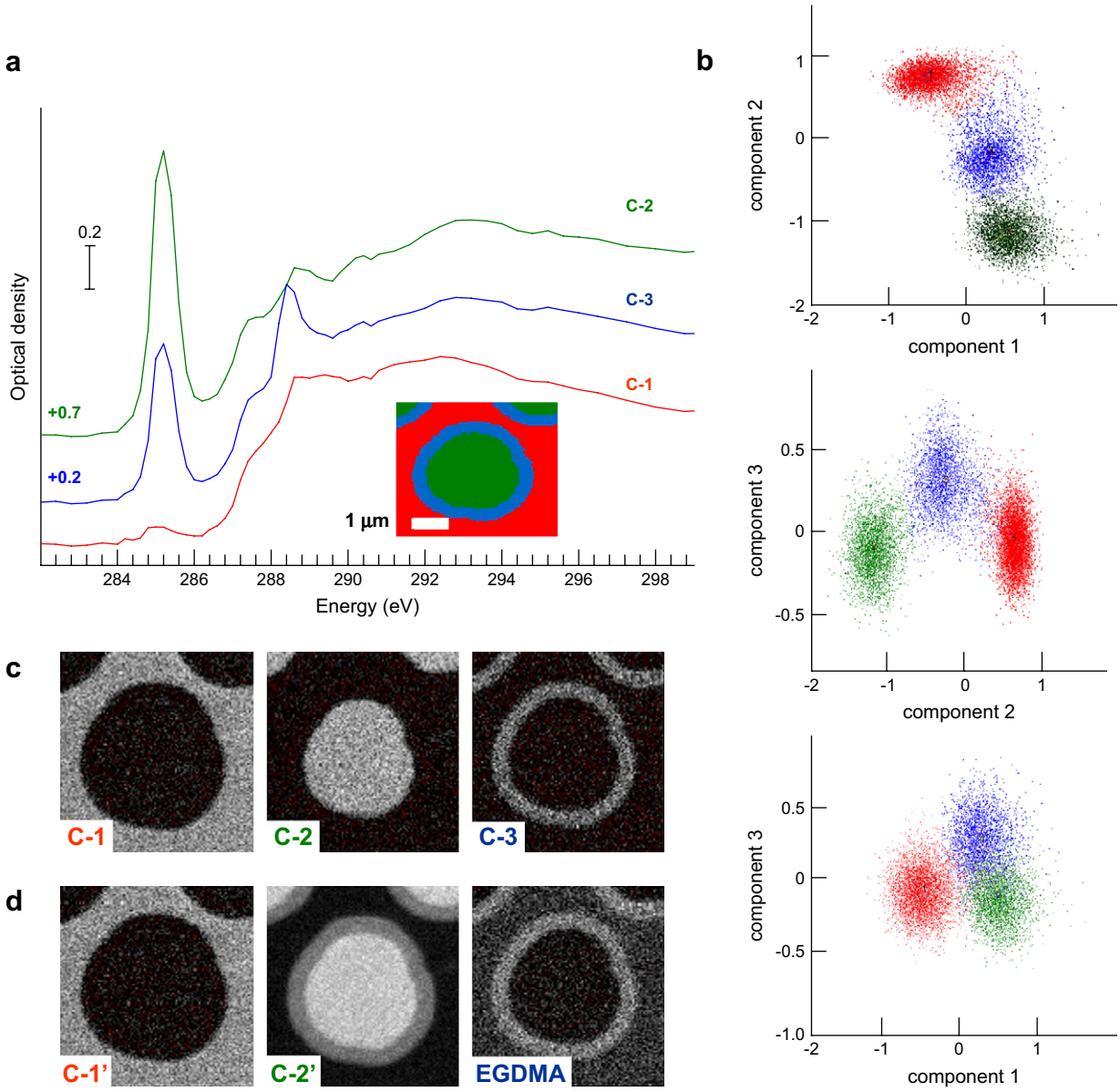

Fig. 17. Result of a multivariate statistical analysis using a combination of principle component and target analysis. (a) Rotated principle components in a three-component target analysis. (b) Cluster plots of PC1 vs PC2; PC2 vs PC3 and PC1 vs PC3. (c) Component maps derived using the C-1, C-2 and C-3 target spectra (Fig. 17a). (d) Component maps derived by replacing C-3 target with the measured spectrum of EGDMA (see Fig. 16a).

products and also construction applications (e.g. the Chunnel). In these applications, competing demands on the materials are made. On the one hand, absorbency of liquids should be maximized. On the other hand, the water absorbed needs to be retained as much as possible under a compressive load. The former is optimized by proper choice of the chemical structure that will absorb the most water and is in many cases an acrylic acid based polymer. The latter requirement necessitates some form of mechanical stiffness. This has been achieved by initially cross-linking the SAP uniformly and more recently, by more heavily cross-linking SAPs near their surface. This cross-linking naturally reduces the swelling capacity. NEXAFS microscopic characterization of surface cross-linked materials initially in the form of beads showed for the first time that the width of the highly cross-linked surface (i.e. shell) is only 5–20 µm [102]. It can also have gradually decaying or surprisingly sharp cross-link density profiles, depending on the fabrication process of these materials. Prior to these studies little was known about the actual cross-link density gradients near the surface regions of these materials. The differences in the density profiles were explained in terms of competing parameters during fabrication, i.e. the diffusion properties of the cross-link agent and the reaction kinetics of the cross-linking process. The diffusion and reaction limited cases result in sharp interfaces or gradual gradients, respectively. In these studies, the contrast between water and the polyacrylic acid based SAP could be substantially enhanced by imaging at 288.5 eV, the photon energy of the C 1s(C═O) → $\pi^*_{C=O}$ transition. Through suitable data analysis a quantitative evaluation of the degree of cross-linking near the edge in

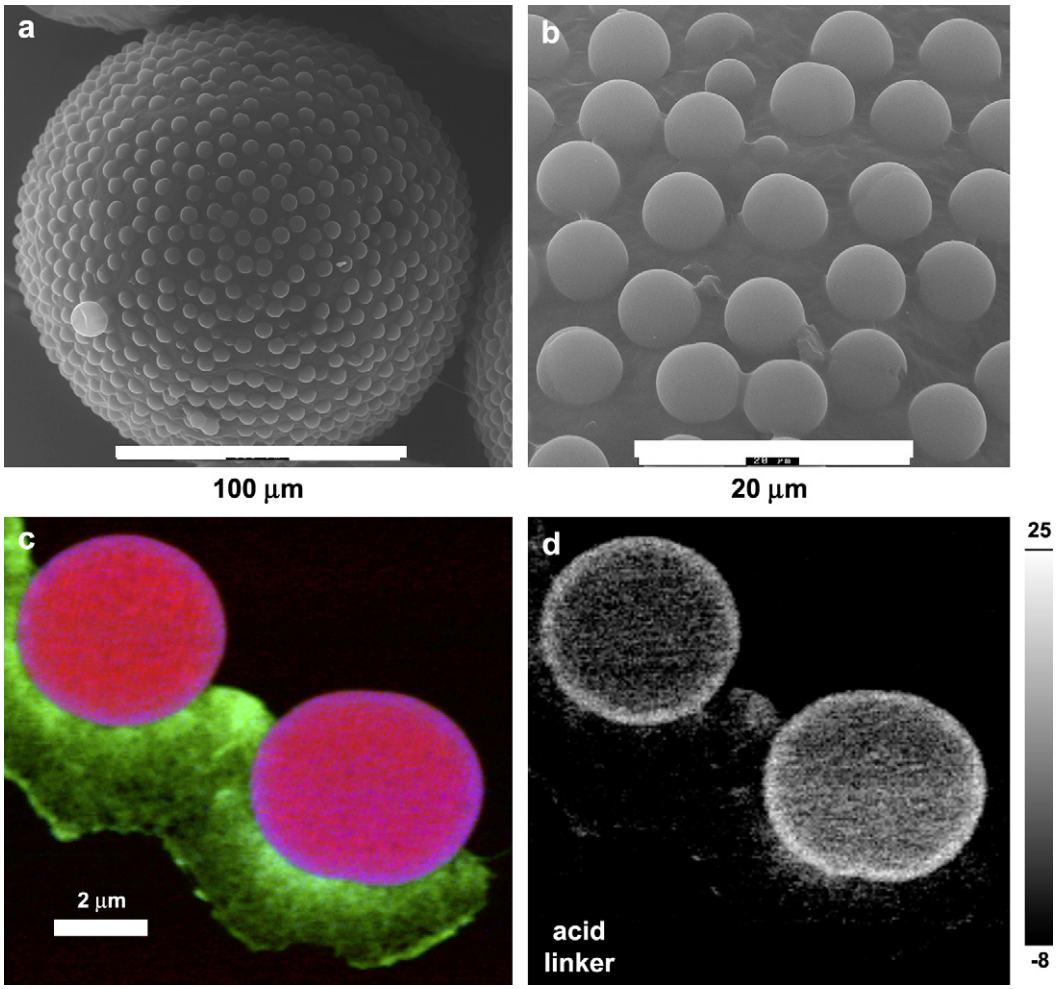

Fig. 18. (a and b) Scanning electron micrograph of a tectocapsule. (c) Color composite of STXM-derived component maps of DVB55 (red), polyurea (green) and maleic anhydride-based acid linker (blue). Due to overlap of the blue acid linker signal with the red DVB55 signal the rim of the DVB particle where the acid linker is concentrated appears purple. (d) Acid linker component map (see Refs. [130,136]).

relation to the cross-link density in the bulk of the material was made. These studies and those of related materials have lead to the optimization of fabrication processes of industrial relevance and on an industrial scale [138].

Under suitable conditions microgels can swell to many times their original volume and hence act like 'nano-sponges', thus offering potential applications in drug delivery, heavy metal sequestration, sensors, catalysis, dynamically tunable microlenses, water purification, as well as viscosity modifiers and smart particulate emulsifiers [137]. Microgels are usually employed in their swollen state, thus *in situ* characterization of these particles under such conditions is desirable for the complete understanding of their behavior and properties. Microgels are microscopic particles that are too small to be visible by conventional optical microscopy, a technique easily adopted for *in situ* applications. Although dynamic light scattering (DLS) can be used to determine the average size of microgel particles and is a very convenient technique for assessing the (de-)swelling of microgels, no direct morphological information regarding aggregation or simultaneous spectroscopic information regarding charge states can be obtained with this sizing technique. In contrast, NEXAFS microscopy can directly image *swollen* and *unswollen* microgel particles in aqueous solutions and characterize their charge state individually *in situ* [137]. Lightly cross-linked poly(4-vinylpyridine)-silica (P4VP-SiO_2) nanocomposite microgel particles were imaged in both their non-swollen (200 nm diameter) and swollen (500 nm diameter) states by adjusting the solution pH. Moreover, spectroscopic analysis across the nitrogen adsorption edge demonstrated that the microgel particles were fully protonated in their swollen state (see Fig. 19). The N 1s → $\pi^*_{N=C}$ transition in P4VP showed a characteristic spectral shift when P4VP was protonated, directly elucidating the underlying mechanism for swelling. More recently, poly(2-vinylpyridine) (P2VP) based microgel particles were characterized at different pH values and salt concentrations [139]. It was directly and simultaneously observed that at low pH the P2VP microgel particles were swollen at low salt concentration but not swollen at high salt concentration, even though P2VP was protonated in both cases. Sufficient salt can screen the charge on the protonated P2VP and thus prevent swelling.

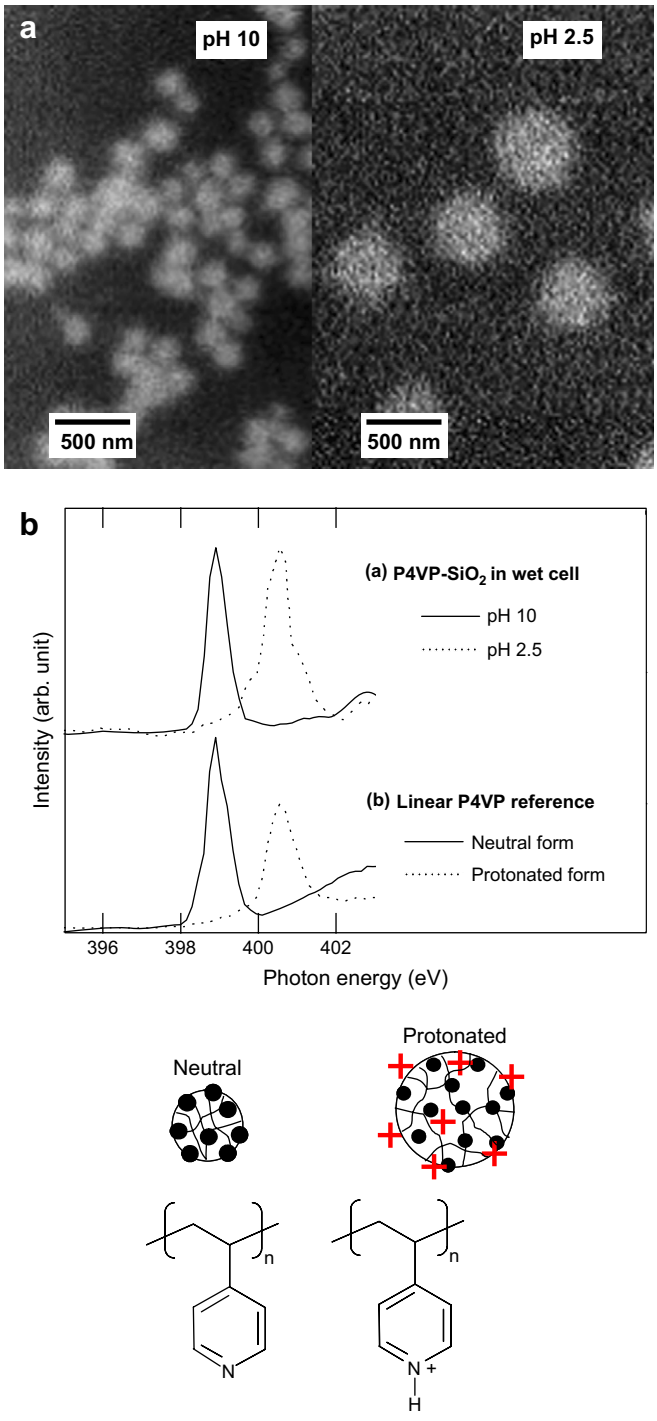

Fig. 19. STXM optical density images of aqueous dispersions of nanocomposite microgel particles in their non-swollen (pH 10) and swollen (pH 2.5) states. NEXAFS spectra (a) of an individual microgel particle and (b) reference spectra at pH 10 and pH 2.5, respectively. (bottom) Schematic of these cationic microgel particles unprotonated and completely protonated at low pH. Figure adopted from Ref. [137].

5.4. Organic electronic materials

Organic light emitting diodes (OLEDs) and organic photovoltaic (OPV) devices fabricated from conjugated polymers are potentially economic alternatives to present device technologies. In order to achieve cost efficiency for these devices, a simple process such as spin-casting or "spray painting" of the active layer will likely have to be employed. Two-component devices fabricated by such methods generally exhibit complicated non-equilibrium structures with phase separation occurring at multiple length scales. It is recognized that the device performance is intimately related to the local composition and morphology of its active components, even for the same overall composition. For example, the work by Shaheen et al. on so-called bulk heterojunction photovoltaic devices demonstrated that optimizing the spin-casting conditions for the MDMO–PPV (poly[2-methoxy-5-(3′,7′-dimethyloctyloxy)-1,4-phenylene vinylene]) and PCBM ((6,6)-phenyl-C_{61}-butyric acid) system results in a significant increase in power conversion efficiency [140]. The use of device function alone as an indicator of process optimization tends to be tedious and a more rational and directed approach based on nanoscale chemical analysis is desirable. In particular, the relation between *local composition* and the *charge carrier and optical properties* should be assessed. The information about performance parameters gained from local optima can then be integrated deliberately throughout the whole device into the next generation of devices. This strategy requires correlative microscopy in which the composition is assessed by NEXAFS microscopy and is correlated, for example, to mapping the current, charge carrier recombination, and energy diffusion [141–143]. This approach might be particularly fruitful for complex device architectures that have more than two components.

The utility of NEXAFS microscopy to this class of materials was first realized in the characterization of the composition and morphology of thin films of blends of poly(9,9-dioctylfluorene-*co*-*N*-(4-butylphenyl)diphenylamine) (TFB) and poly(9,9′-dioctylfluorene-*co*-benzothiadiazole) (F8BT), materials that are used in organic LEDs. Spun-cast thin films ranging in thickness between 65 nm and 150 nm were investigated. The NEXAFS spectra from TFB and F8BT and compositional maps of F8BT and the corresponding SPM images of a 150 nm thick film were already shown in Fig. 1 [29]. As noted above, the spectral differences between TFB and F8BT are relatively large, even though superficially, similar chemical functional groups are in both materials in similar ratios. Part of the spectral differences are due to the more extensive broadening of the conduction band in F8BT, with a pronounced shoulder at the relatively low energy of 284.4 eV. Regarding the blend's morphology, little lateral variation in composition was found within the enclosed TFB domains. In contrast, the F8BT concentration in the F8BT-rich regions is >90 wt% near the domain interface (Fig. 1a) and falls to 60 wt% away from the interface and into the domain. The enrichment of the domain interface with F8BT, which facilitates efficient charge transport, and the interface sharpness, which promotes charge capture and recombination, help explain the efficient performance of TFB:F8BT-based LEDs. This application provided novel information about these devices by correlating composition to relevant electronic processes. It demonstrates the potential of NEXAFS microscopy for this class of materials and type of application.

MDMO–PPV:PCBM blends [144] and poly(9,9′-dioctylfluorene-*co*-bis-*N*,*N*′-(4,butylphenyl)-bis-*N*,*N*′-phenyl-1,4-phenylene-diamine) (PFB) blended with F8BT [145] are some of the other organic electronic heterogeneous systems investigated with NEXAFS microscopy to date. New developments are also underway to measure the soft X-ray induced device current (SoXBIC) from a fully active device that is specially fabricated such that also a sufficient number of X-rays are transmitted to allow the local composition to be determined. This will allow to directly relate the local device composition to local device efficiency. First results that demonstrate the feasibility have been achieved [146]. Given the importance of organic devices, numerous applications to this class of materials can be readily foreseen, particularly as the spatial resolution of NEXAFS microscopy approaches 10–15 nm. This is the length scale that matches the exciton diffusion lengths in these materials, and hence the ideal length scale of the in-plane morphology in OPV thin film heterojunction devices.

5.5. Biomaterials: X-PEEM and STXM studies of protein adsorption on polymers

Biomaterials are typically polymers, either in the bulk, to form structures with desired mechanical properties (e.g. flexible dialysis tubes), or as coatings, to provide specific chemical properties (protein repellency, selective protein binding, etc). Optimization of polymer systems to achieve biocompatibility while providing necessary structural support and flexibility is a very active area of research. Both STXM and X-PEEM are being used to investigate biomaterials, both in terms of their intrinsic bulk and surface properties, and also to characterize their interactions with biological entities such as proteins and cells. STXM can be applied to samples in a fully hydrated environment, and thus can be used to investigate samples under a layer of buffer or nutrient solution, close to actual biological conditions. However, X-PEEM has much greater surface sensitivity and thus has so far been the technique most frequently used in imaging proteins at the submonolayer levels relevant to investigations of preferential adsorption on laterally phase segregated polymer substrates.

STXM was used to study adsorption of fibrinogen (a blood protein) on a polyurethane reinforced with styrene–acrylonitrile (SAN) and poly-isocyanate poly-addition (PIPA) filler particles [94]. For samples investigated dry, rehydrated with deionized water, and even under a buffer solution of 0.01 mg/ml fibrinogen, the fibrinogen was found to be preferentially adsorbed at the interface of the SAN particles and the polyether-rich matrix. Annealed (160 °C, 8 h) spun-cast thin films of (30:70 w/w) blends of polystyrene (PS, 312 kDa) and polymethyl-methacrylate (PMMA, 1.1 MDa) are used as model substrates for both X-PEEM and STXM studies of preferential attachment of both fibrinogen and human serum albumin. The morphology and surface chemistry of the PS/PMMA substrate have been investigated extensively by STXM, X-PEEM and AFM [96]. The location of fibrinogen (Fg) on this PS/PMMA surface when adsorbed during a 10 min or 20 min exposure from deionized water or from phosphate buffer at physiological pH at concentrations from 0.005 mg/ml up to 1 mg/ml has been mapped using X-PEEM [147]. Radio-labeling studies showed that there is a thermodynamic preference for PS relative to PMMA. When the fibrinogen was adsorbed from phosphate buffer solution, it was found preferentially on the PS domains. However, when either fibrinogen or albumin is adsorbed from a non-buffered aqueous solution they adsorb preferentially at the PS/PMMA interface [78,147]. This has been determined to be a kinetic preference since longer time exposures have found a redistribution of the albumin to form a distribution with similar amounts on the PMMA and PS domains [78]. More recent X-PEEM studies [148] have shown that there is a significant dependence of the adsorption site preference on the pH of the solution (2–10). Fig. 20 displays results from this study. At neutral, very low and very high pH there is a strong preference for the interface and PS domains. However, at pH 4.0 where albumin is known to start to unfold, the amount on the PMMA domains increases significantly. In contrast at pH 8.6, where the protein takes its most compact form, the amount of protein adsorbed drops significantly, and that which does adsorb strongly prefers the interface. These site preferences can be rationalized in terms of the known changes with pH in the albumin structure and thus the hydrophobic/hydrophilic character of the protein surface [148]. STXM has also been used to examine albumin adsorption on PS/PMMA surfaces with results that are in agreement with the X-PEEM results [147].

5.6. Dichroism

5.6.1. Kevlar and biofibers

Synthetic fibers and natural biopolymer fibers are often anisotropic. Understanding this anisotropy and the underlying spatial organization often leads to improved understanding of the fiber's mechanical characteristics. Similar to IR dichroism microscopy, X-ray linear dichroism microscopy in an STXM provides a powerful tool to investigate these fibers. Again the spatial resolution is more than an order of magnitude better with X-rays than with IR. The first application of linear dichroism microscopy revealed the qualitative radial alignment of various functional groups in Kevlar™ fibers [12]. The subsequent quantitative comparison of different Kevlar® fiber grades determined that Kevlar® 149 is about 1.6 and 2.3 times as oriented in the radial direction as Kevlar® 49 and Kevlar® 29, respectively [52]. These values can then be used to explain, at least partially, the torsional and tensional properties of these fibers.

Amongst natural fibers, spider silk is widely recognized as having mechanical properties – specifically the combination of strength and elasticity – which are far superior to any synthetic fiber. To date, the origin of these properties is not fully understood. The microstructure of the silk filament, which is typically a single protein, is controlled in part by its amino acid sequence and in part by the conditions under which the fiber is spun. The fibers are formed from an aqueous protein solution in a complex spinning apparatus where variations in pH and the concentration of specific ions, as well as various

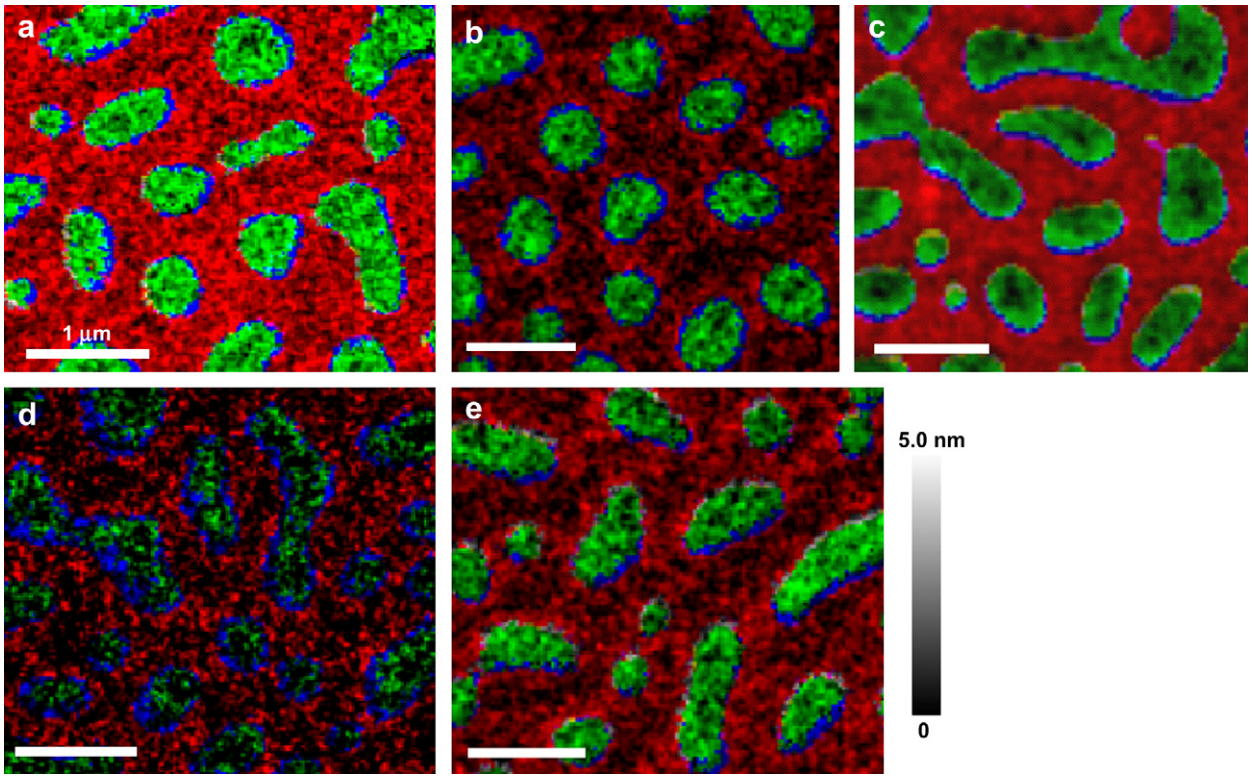

Fig. 20. Colorized albumin component maps derived from C 1s X-PEEM of albumin adsorbed from solutions of pH: (a) 2.0, (b) 4.0, (c) 7.0, (d) 8.6, (e) 10.0. The signal from the PS/PMMA substrate has been used to segregate the area into PS, PMMA and interface regions. Each region of the albumin component map has been extracted, colorized and re-assembled. The intensity of each color (red – albumin on PS, green – albumin on PMMA, blue – albumin on interface) gives the local thickness on a 0–5 nm scale (from Ref. [148]).

mechanical actions in the extrusion process control chain–chain interactions, alignment and supramolecular structure. This leads to molecular orientation at different length scales, which ultimately determines the mechanical properties of the resulting silk. A detailed understanding of silk microstructure is highly motivated by industrial efforts to produce synthetic fibers that biomimic spider silk's strength and toughness. The Hitchcock and Pezolet groups are collaborating to use STXM and microRaman to systematically investigate the microstructure of natural and synthetic silks. In particular the dichroic NEXAFS signal is measured in detail using azimuthal scanning of samples in STXM [97]. Fig. 21 illustrates STXM mapping of β-sheet distributions in a longitudinal section of a dragline spider silk fiber obtained from a *Nephilia clavipes* spider under controlled slow pull conditions [97,99]. Novel aspects learned from X-ray microscopy, which help understand why spider silk has such amazing mechanical properties, include a region of enhanced orientational order at the skin of the fiber, and the presence of an apparently random distributions of more oriented β-sheet crystallites, interspersed with amorphous regions. This type of stiff reinforcement within a flexible matrix is a common motif to achieve high strength yet flexible materials.

5.6.2. Semi-crystalline thin polymer films

The mechanical and electrical responses of thin films of crystallizable polymers are empirically known to vary with film thickness. This in turn influences the utility of these films as sensors and actuators [149]. A study panel has concluded in 2003 that "little is known either theoretically or experimentally about crystallinity in thin films" [149]. Even bulk crystallization is "still intensely debated" [149,150]. A few model thin film systems have been explored, yet the results are seemingly contradictory and some of the controlling parameters still seem to be "hidden". This appears to be similar to the situation that involves the thermal properties of thin films, such as changes in glass transition temperatures T_g. Only after extensive studies did a more comprehensive understanding of T_g changes in thin films emerge. In order to address some of these fundamental questions in semi-crystalline thin films, the melting and morphological properties of linear medium and linear low density polyethylenes (LMDPE and LLDPE, respectively) have been investigated with SPM and X-ray methods [151,152]. STXM imaging and NEXAFS spectroscopy revealed an edge-on lamellae (C–C backbone in-plane) to flat-on lamella (C–C backbone normal to surface) transition for very thin films (see Fig. 22). The thicker films have spherulitic-like crystallites, whereas the thinner films show a markedly different morphology that corresponds to flat-on lamellar orientations [152]. The NEXAFS spectra recorded from different parts of the sample and their specific dichroic nature allow clear assignment of the orientation of the carbon backbone to have either primarily in-plane (edge-on) or out-of-plane (flat-on lamellae) orientation. Substantial suppression of the

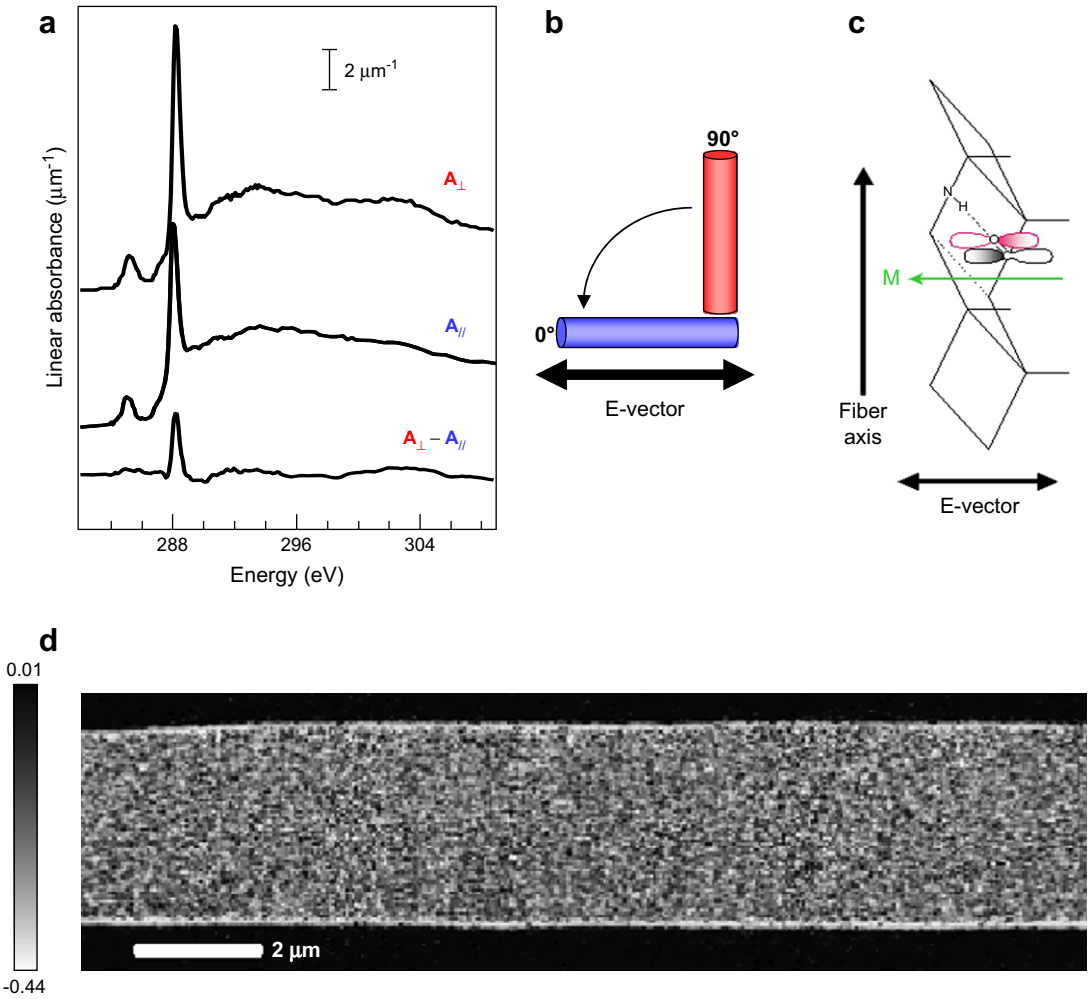

Fig. 21. Spider silk orientation mapping from the C 1s → π* linear dichroic signal (azimuthal angular dependence). (a) Spectral change with change in fiber orientation, as indicated in (b). (c) Direction for C 1s → π* transition moment in β-sheet region. (d) Orientation of map of angles of $\langle P2 \rangle$ orientation parameter, derived from the amplitude of the dichroic signal [97,99].

melting temperature as a function of film thickness has also been observed in these LMDPE and LLDPE thin films [152]. Details of the observed morphologies and the depth of melting temperature suppression were dependent on the substrate utilized. SPM characterization alone would have not been able to clearly assess the differences in the orientation and organization of crystallites as a function of film thickness.

5.6.3. PET/Vectra™ blends produced by mechanical alloying

The incorporation of liquid crystalline polymers such as Vectra™ into commodity thermoplastic polymers such as poly(ethylene terephthalate) (PET) has the potential to significantly improve barrier properties to gases at relatively low cost. Such an incorporation, one that would combine the thermal processability of PET with the high barrier properties of Vectra™ remains, however, an on-going engineering challenge towards high-performance, low-cost polymeric blends. Smith et al. investigated if mechanical alloying is a process strategy that can accomplish blending of polymers with such diverse mechanical and thermal properties [122]. Blends of PET and Vectra™ A950 (73/27 mol% oxybenzoate/2,6-oxynaphthoate) were produced, varying in composition from 75/25 to 99/1 by wt%. The mechanically alloyed blends were subsequently melt-pressed and sectioned for investigation of the produced morphology as an indicator of process efficacy. Similar to the materials and appropriate choice of characterization tool mentioned above, the PET/Vectra™ system is difficult to stain and has little contrast in TEM, yet exhibits large natural contrast in NEXAFS microscopy. Fig. 23 shows the X-ray micrographs of a 99/1 w/w PET/Vectra™ blends imaged at a photon energy of 286.7 eV. The contrast between the Vectra™ dispersions and the PET matrix is due to the compositional sensitivity of NEXAFS microscopy. Some of the contrast within the larger Vectra™ domains in the individual images (Fig. 23a and b) arises from molecular orientation and thickness variations. The dichroic ratio image (Fig. 23c), derived from the two orientations displayed in Fig. 23a and b, cancels thickness and compositional effects revealing that anisotropic orientation inside Vectra™ domains is only observable in domains larger than about 2 μm. The frequency and size of the Vectra™

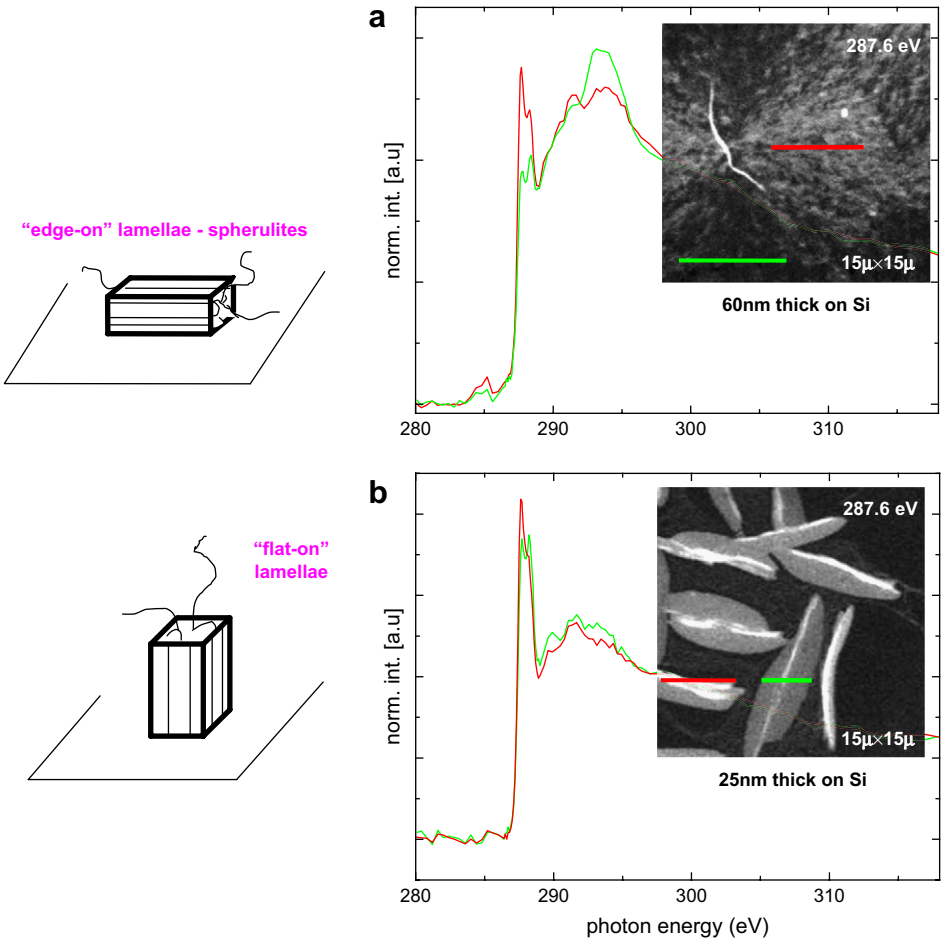

Fig. 22. STXM images and NEXAFS spectra of medium density PE thin film on silicon substrate; (a) 60 nm thick and (b) 25 nm thick. The PE thin films show a transition from edge-on to flat-on lamellae below a critical thickness of ~30 nm, schematically indicated on the left. (Adopted from Ref. [152].)

dispersions increased with increasing Vectra™ concentration [122]. The presence of small, 100 nm Vectra domains demonstrated that mechanical alloying is capable of pulverizing Vectra™. The PET/Vectra™ blends retained much of their initial degree of mixing during melt post-processing. NEXAFS spectroscopy from selected areas and domains also showed that the Vectra™ domains contained little, if any PET. NEXAFS microscopy thus allowed this system to be

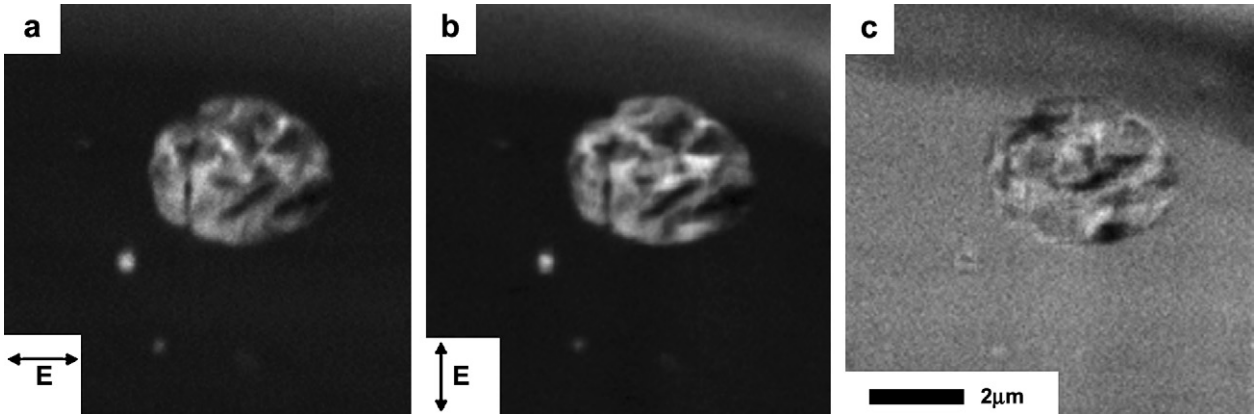

Fig. 23. NEXAFS images acquired at 286.7 eV of a 99/1 w/w PET/Vectra™ blend cryo-milled and subsequently melt-pressed. Images (a) and (b) have been converted to optical density. In images (a) and (b), the electric polarization vector ($\vec{E}$) is rotated by 90° with respect to each other, as indicated. Changes in the relative intensity in these images are primarily due to anisotropic molecular orientation. (c) Ratio of these images, revealing the linear dichroism of the specimen. Small Vectra™ domains appear gray and possess no discernible orientation, whereas the large dispersion exhibits a measurable degree of molecular orientation (black and white areas) due to the nematic nature of this liquid crystalline polymer [122].

characterized and the results related to the processing conditions. Even though the PET/Vectra™ system is one of the earlier NEXAFS microscopic applications, it was included here as an instructive example regarding the capabilities of NEXAFS microscopy since it combines chemical and orientational analyses in a heterogeneous sample at high spatial resolution.

6. Scattering/reflectivity applications

RSoXR and RSoXS are very nascent techniques with a limited number of applications to date and the reader cannot be pointed to extensive reference materials in the literature. To exemplify their capabilities and principles, we focus first on PS/PMMA bilayers as a model system. Using a subset of the same soft X-ray photon energies used in the simulations shown in Fig. 10, the reflectance from a 15 nm/42 nm PS/PMMA bilayer was recorded (see Fig. 24) [27]. The film thicknesses were close to the 1:3 ratio used in the simulation. The same strong photon energy dependence was observed experimentally as predicted by the simulations. At ~14.2 keV, only fringes corresponding to the total layer were observed due to the low sensitivity to the polymer/polymer interface at this energy. In contrast, strong modulations in the amplitude of these reflectivity fringes (also referred to as beats) for photon energies of 270.0 eV, 285.2 eV, and 288.5 eV directly demonstrate high sensitivity to the polymer/polymer interface. The vertical markers in Fig. 24 delineate two sets of four fringes (270 eV data) with $\Delta q \approx 0.11\ \mathrm{nm}^{-1}$, which corresponds to $d = 57$ nm, i.e. the total film thickness. Weaker beats are observed at 280 eV and 283 eV, for which the reflectance appears to have only three fringes between markers. The average fringe spacing at 280.0 eV and 283.4 eV is $\Delta q = 0.15\ \mathrm{nm}^{-1}$, and corresponds to the PMMA layer thickness of $d = 42$ nm. This is not surprising as these are photon energies where δ of PS is very close to zero and thus the top surface reflects very little. This is corroborated by inspection of the low q range of the data sets that shows that the critical angle gets smaller from 270.0 eV to 280.0 eV, and disappears entirely for 283.4 eV due to $\delta < 0$ for the top PS layer at that energy, i.e. $(1-\delta) > 1$. This clearly indicates that δ has a zero crossing at an energy between 280.0 eV and 283.4 eV. This is in good agreement with the calculated δ plotted in Fig. 8. Additional subtleties about these data in relation to the optical constants of the materials are discussed by Wang et al. [27].

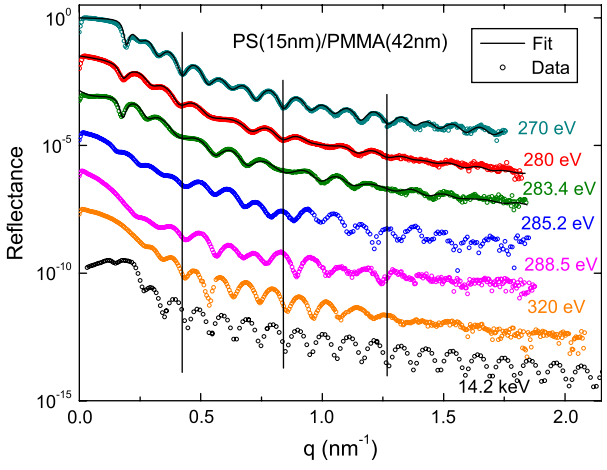

Fig. 24. Experimental data (circle) of 15 nm/42 nm PS/PMMA bilayer acquired at 270 eV, 280 eV, 283.4 eV, 285.2 eV, 288.5 eV, 320 eV and 14.2 keV and fits (solid line) for 270 eV, 280 eV and 283.4 eV [27].

The information about the individual film thickness and the interfacial width is encoded by the amplitude modulation of these fringes and their change as a function of q. The roughness or chemical diffuseness of an interface, σ, reduces the reflectivity at the interfaces by a roughness factor $\exp(-2k_{zi}k_{zj}\sigma^2) \approx \exp(-q^2\sigma^2/2)$, where k_{zi} and k_{zj} are the perpendicular components of the wave vectors in medium i and j, respectively. The effect of the roughness factor and the q-dependence allows the interfacial roughness and width to be measured with substantially sub-nanometer precision. This is below the wavelength limit $\lambda/2$, a criterion that applies to the minimum thickness of a layer that can be probed. Due to the strong and tunable sensitivity to both the PS/vacuum and PS/PMMA interfaces, RSoXR can measure the surface and interface roughness simultaneously and independently with high precision. Hence, fitting the profiles and extracting surface, σ_s, and interface, σ_i, width/roughness values will be highly accurate without the need to fix the surface roughness as an ad hoc input parameter to the fit or to provide it from an independent measurement [27].

A direct comparison of the same PS/PMMA bilayers characterized with neutron reflectivity, conventional X-ray reflectivity, and RSoXR was performed in order to provide a context for RSoXR to existing characterization methods [27]. These methods were compared and contrasted in terms of the relevant operating parameters and sensitivity. Sufficient contrast in RSoXR for PBrS/PMMA, PS/P2VP, PS/SAN and PCHMA/PMMA bilayer systems was also demonstrated. Furthermore, an anomalous isotope effect in the PS/PMMA system has been confirmed. In segregation experiments characterized with SIMS, it had been previously shown that dPS segregated to an hPS:dPS/hPMMA interface even though bulk χ parameters would have predicted a depletion of dPS [153]. The RXR measurements have confirmed the anomalous behavior in this system by measuring interfacial widths for dPS/hPMMA that were consistently ~15% to 25% larger than for hPS/hPMMA, directly confirming that dPS/hPMMA has a lower interfacial tension than hPS/hPMMA [154]. The thermodynamics of the PS/PMMA interface can thus not be predicted from the bulk interaction and mean field theories.

The bond-selective contrast mechanism exemplified above for RSoXR can, of course, also be used in non-specular geometries (RSoXS). RSoXS was first successfully utilized in transmission. An enhancement in sensitivity was demonstrated through the use of a heterogeneous, two-phase polymer film for which hard X-ray and neutron scattering of non-deuterated materials lack sensitivity due to low contrast [15]. The polyphenylene based films are used for insulating applications in integrated circuits and had aromatic porogen particles

dispersed in it [155]. The porogen decomposes during curing, leaving behind a film with voids that has improved dielectric properties. Ideally, a nano-porous film with a large void to matrix volume ratio yet great strength is produced. Understanding the pore formation process and its limitations requires comparison of final pore sizes with original porogen sizes, i.e. size distributions before and after processing. The NEXAFS spectral differences for the two materials used were rather small and are shown in Fig. 25a. Spectral differences this small would have made it difficult to achieve good contrast and good S/N in NEXAFS absorption microscopy for such small particles, even if the required spatial resolution would be available. In contrast, sufficient scattering occurs, partially on account that many particles get sampled simultaneously and a much higher total photon flux can be used in scattering, without concern of radiation damage. Also, scattering is a low background technique, whereas transmission NEXAFS for thin films has a very high background. Scattering data from a phase-separated film of the same two materials whose spectra are shown in Fig. 26b reveal significant scattering intensity enhancements, i.e. contrast, at energies adjacent to the C 1s → $\pi_{C=C}$* resonance and at higher energies (see Fig. 24). Overall, there is very good agreement between the calculated and measured scattering intensity. The size and size distribution of the porogen before and after void formation could thus be characterized, yielding the important insight that the smallest porogen particles, ~4 nm in size, lead to voids that are unstable and cavitate [15]. Use of porogen particles smaller than 4 nm would therefore not yield any further improvement in dielectric properties as the mechanical stability of the polyphenylene based matrix cannot support such small voids.

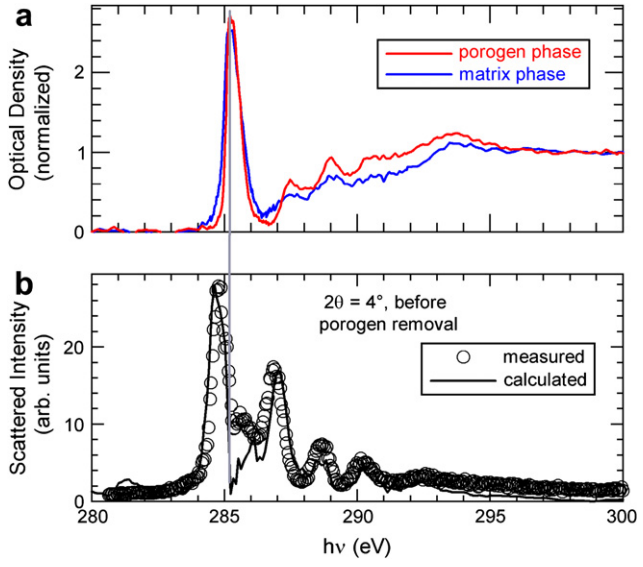

Fig. 25. (a) Absorption spectra of two polymer phases each having a dominant C 1s → $\pi_{C=C}$* resonance. (b) Scattering spectra from a phase-separated film of the same two phases showing significant resonant enhancement adjacent to the C 1s → $\pi_{C=C}$* resonance and at higher energies. (Figure courtesy of G. Mitchell. Reproduced from Ref. [15].)

The application range of RSoXS was extended from spherical particles with low contrast to structured nanoparticles [14] in a study that showed that the effective radius of particles with an overall skin–core structure as observed by scattering depended on the photon energy utilized. Two structured, styrene-acrylic polymer composite latex particles ~230 nm in diameter were characterized. The photon energy-dependent scattering plots for PMMA/P(BA-*co*-S) and P(MA-*co*-MMA)/PS particles and TEM images of them are shown in Fig. 26. The PMMA/P(BA-*co*-S) scattering in Fig. 26c shows strong photon energy dependence. At a photon energy of 285.2 eV the styrene in the outer "shell" contributes strongly and the particle has a larger effective radius than at 288.4 eV, an energy for which the PMMA core contributes strongly to the scattering. The situation is markedly different for the P(MA-*co*-MMA)/PS. The data at 285.2 eV, 288.4 eV, and

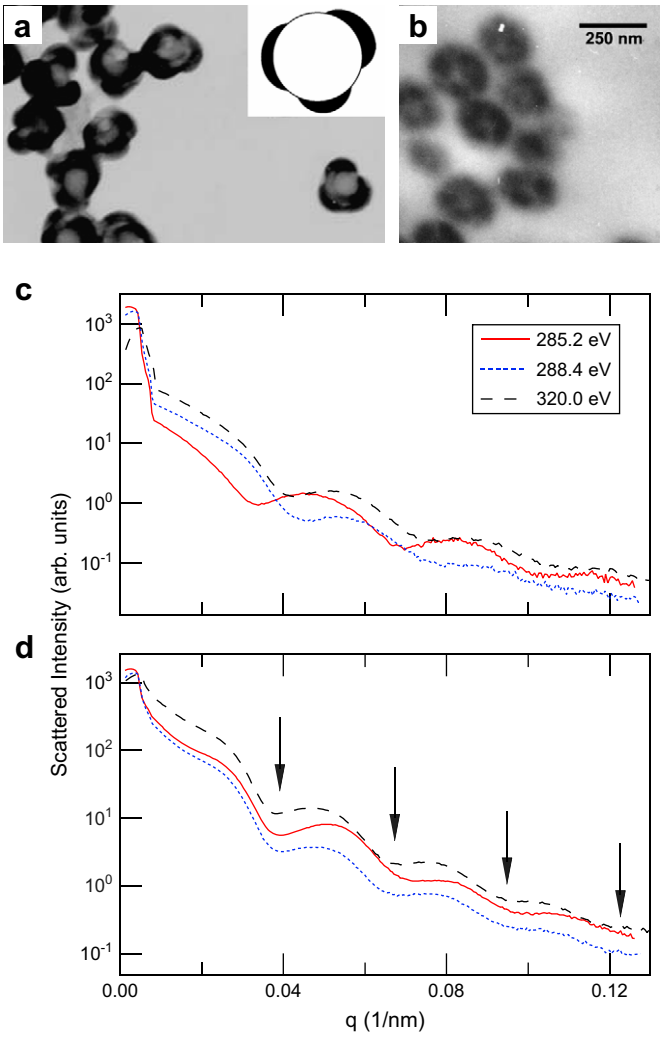

Fig. 26. (a) TEM image of sectioned PMMA/P(BA-*co*-S) and schematic of idealized particle. (b) TEM image of sectioned P(MA-*co*-MMA)/PS. Scattered intensity of (c) PMMA/P(BA-*co*-S) and (d) P(MA-*co*-MMA)/PS at 285.2 eV (solid) 288.4 eV (dotted) and 320 eV (dashed). The theoretical scattering minima of dispersed ideal spheres of radius R (occurring for $qR = 4.5$, 7.73, 10.9, and 14.1) are indicated for $R = 115$ nm. This radius matches well with the independently derived size for these P(MA-*co*-MMA)/PS particles [156].

320 eV do not show large variations, indicating that the composition in these particles is much more homogeneous. This average radius matches well with the independently derived size for these P(MA-*co*-MMA)/PS particles [156]. The conclusion about the differences in the compositional distribution could be drawn without having to consider any models, simulations, or detailed analysis of a form factor.

In general, the availability of scattering profiles at several different energies should constrain structural models of the samples better than if only a single profile is used, as is the case for neutron or hard X-ray scattering.

Multilayer systems based on PS-*b*-PMMA block copolymers were also investigated and were shown to have excellent contrast over a large energy range and for very thick films [27,157]. RSoXR has also been used to study thin film PI-*b*-PS copolymer samples [28].

7. Discussion and future perspectives

This overview has presented the basics of soft X-ray microscopy and resonant scattering as applied to macromolecules and outlined a number of examples to illustrate the breadth and capabilities of these techniques. While NEXAFS microscopy is a much more established technique than RSoXS and RSoXR, the latter two are reciprocal space methods that are complementary to NEXAFS microscopy and have their own set of advantages. Indeed, RSoXR and RSoXS were developed explicitly to provide chemically sensitive information on size scales that the real-space X-ray techniques, i.e. STXM and TXM, cannot currently achieve or for which the real-space methods impart too much radiation damage. In addition, the averaging over a large ensemble of similar systems provided by RSoXR and RSoXS is sometimes an advantage rather than a disadvantage in the characterization of materials.

Like any characterization tool, NEXAFS microscopy and RSoXS have not only unique strengths but also limitations. The strengths should be clear from the discussion and applications described above. RSoXS is such a recent development that its limitations remain largely unexplored and undefined. To complement the sections above that are primarily informed by strength and capabilities, we will summarize below the limitations of NEXAFS microscopy and the corresponding possible solutions. Frequently, these limitations intersect with the instrument and method developments already underway if the limitations are technological rather than physical in nature.

7.1. Radiation damage

The most common radiation damage outcomes relevant to NEXAFS microscopy and RSoXS comprise primarily chemical modifications and mass loss. These modifications limit the compositional accuracy achievable and thus undermine one of the key advantages of these methods. Damage is mitigated in RSoXS by spreading the dose over a relatively large sample area and the ensemble of the structures to be studied. Unfortunately, details of the spatial relationships of unique structures in the sample are then lost. In NEXAFS microscopy, measuring and knowing the damage rate of the most easily damaged component will allow the selection of an acquisition strategy (point, vs. line vs. stack; defocus wherever compatible with spatial scale of structures of interest; etc.) so the dose is less than a fraction of its critical dose [107,108]. Some of these strategies employed in NEXAFS microscopy are equivalent to averaging over ensemble averages or the degradation of the effective spatial resolution, although automated procedures to group together regions of identical chemical character to build statistics provide a means to preserve the spatial resolution. The information content per critical dose strongly depends on the radiation sensitivity of the polymers used (which can vary by three orders of magnitude [108]) and the contrast, i.e. relative difference of the NEXAFS spectra of the components, of the system investigated. Wet systems at room temperature damage faster than dry systems due to the diffusion of radicals [158]. One uses wet systems only when that sample environment is really required and the extra sensitivity to damage cannot be entirely avoided. It can be somewhat mitigated by the use of radical scavengers [158]. The increased sensitivity simply means that extra attention needs to be paid to damage artifacts. Cryo techniques are often used in TEM and even XRM to mitigate damage. However, cryo only limits mass loss and thus preserves structures and morphology. It does not preserve the chemistry and hence the spectroscopic analysis capabilities [110]. The fundamental limits of damage per core excitation ultimately dictate the achievable signal-to-noise (S/N) ratio. The damage limit strongly depends on the material, their differential NEXAFS spectra, and the sample thickness used (S/N in transmission is a strong function of thickness). Generally, aromatic materials are less sensitive and provide high contrast. Polyolefins, acrylates, and polyols are very radiation sensitive. The spatial resolution achievable in the latter polymer systems will be limited to >10 nm.

7.2. Spatial resolution

Many polymer problems – e.g. block copolymer nanostructures – require resolution better than currently achievable with NEXAFS microscopy, but are well within the capabilities of RSoXS. RSoXS presently has good S/N to about 1 nm^{-1}, a momentum transfer value that corresponds to a spatial resolution below 5 nm. Further improvements to the spatial resolution in STXM will depend on on-going efforts to improve zone plate technology and to improve the mechanical scanning and navigation technologies. Adoption of the 15 nm outermost zone width zone plates used in a TXM [72] for use in an STXM will result in $\sim$15 nm spatial resolution for the latter. Efforts are underway to achieve 10 nm outermost zone width zone plates. The resulting 10–15 nm resolution would allow STXM to enter a regime where even block copolymer systems can be investigated. For surface investigations, aberration corrected optics in X-PEEM will achieve very high resolution [58,59]. As discussed above, a system dependent fundamental physical limit of $\sim$10 nm might be set by radiation damage.

7.3. Space/sample environment constraints

Many applications require *in situ* modification for stimulus/response studies (e.g. electrochemistry, chemical reaction, solvent effects, humidity effects, tensile strain, etc.). The working distance in a present day STXM is only ~150 μm, often limiting simple mechanical implementations of the required modifications of the sample mounting. Ingenuity can conquer these problems in many cases, and solutions are already available to control temperature, stress, chemical reaction [159], electrical potential [160], magnetic fields [161], humidity, and soft X-ray beam induced current measurements [146]. In fact, the challenges in NEXAFS microscopy are probably less severe than in TEMs, for which many effective solutions have already been found. Many of the TEM solutions can be adopted or extended for use in NEXAFS microscopy.

7.4. Imaging modality

Some systems require three-dimensional (3D) characterization, i.e. tomography, and not just a two-dimensional projection. TXM does tomography well in ''imaging'' mode, but only with limited spectral information. Recently, angle scan STXM tomography at multiple energies (i.e. 3D chemical mapping) has been developed [162,163], extending NEXAFS microscopy capabilities.

7.5. Sample contamination

Most existing STXM microscopes are using hydrocarbon lubricated stages which can contaminate samples with compounds derived from these lubricants deposited as a consequence of radiation damage. This can degrade the accuracy of compositional analysis if irradiation times used are long enough for the contamination to become significant. Several efforts to switch to UHV enclosures and ultra-clean all-piezo stages for STXM are in progress.

7.6. Sample limitations

Ultramicrotomy of some systems – especially hard/soft combinations – is a challenge. Again, the TEM community has developed excellent techniques to cope with these challenges, many of which can be adopted or extended for work with X-rays. However, TEM techniques such as ion milling might modify the sample to such an extent that the analytical capabilities of NEXAFS microscopy are compromised. Also, embedding porous materials can have serious drawbacks or cause complications. The embedding material might confound the compositional analysis that one is seeking.

7.7. Data acquisition rates

Present STXM acquisition times for good images are on the order of minute. However, the current sample scanning devices used to make images cannot take full advantage of the high flux in STXMs on undulator beamlines at third generation sources (ALS, CLS). New scanning devices promise an improvement by a factor of 5–10 in speed, achieving near-video rates for small areas. This expands both the scientific capabilities and the total number of applications that could be accomplished (typically, STXM user time is heavily oversubscribed).

7.8. Charging in PEEM

Most polymers are not very good conductors. In a PEEM, photons liberate photoelectrons and if the associated charges are not replaced, the sample will charge positively. This can lead to a complete loss of the imaging capabilities of PEEM. Charging can be prevented in most polymer systems by very thin metal coatings or by the use of ultra-thin samples (<150 nm). The latter are typically prepared with casting methods, as the transfer of ultramicrotomed sections on a substrate leads to substantial topography artifacts in PEEM. Vacuum degradation is also a limiting factor for some systems.

Access to STXM (and PEEM) facilities is growing steadily and with an accelerating pace. Whereas the first STXM was operated at a relatively low brightness bending magnet beamline at the National Synchrotron Light Source (NSLS) UV ring in the 1980s [164], very respectable performance can be achieved with the use of high-brightness bending magnets at third generation synchrotron facilities such as the ALS or Swiss Light Source [21]. Furthermore, a number of STXMs are now operating using linear [165] or elliptically polarized undulators (EPU) [21,166,167]. Additional STXMs are under design, construction, or planned at BESSY-II (Berlin, Germany), Soleil (Paris, France), SSRL (Stanford, USA) and the Shanghai synchrotron, amongst other locations. These new facilities will allow many more users to utilize these powerful techniques.

Although RSoXS is a very recent development, plans are being developed for a dedicated facility at the ALS. We are optimistic that the new capabilities of RSoXR and RSoXS afforded to the polymer community will cause the field to grow solidly in the near future.

Acknowledgements

We acknowledge fruitful discussions and help from Ed. Rightor, Gary Mitchell, Andreas Scholl, Rainer Fink, Chris Jacobsen, Cheng Wang, and Shuming Hu. The P(S-*r*-AN) samples utilized for Fig. 7 were provided by Ed. Rightor with data acquired at the X1A STXM at the NSLS.

Appendix A

To complement the case studies detailed above, a short description of most of the additional NEXAFS microscopy applications to date not mentioned above in the application section follows below, grouped in broad categories. The focus is on materials and nano science related applications relevant to this journal and this summary does not include a comprehensive listing of applications in other subfields. These can be

found in Supplementary material. A brief summary of what has been learned from the NEXAFS microscopy characterization is provided for most of the work cited.

Homopolymer or binary polymer thin film morphologies and surfaces: polymer thin films and interfaces play a vital role in a number of technologies and are studied extensively with a range of powerful techniques to understand their fundamental character and behavior (e.g. Ref. [2]).

- The orientation of polymer chains in polyimide surfaces rubbed with a stylus was characterized with PEEM and the critical pressure required for alignment was determined by measuring the width of the tracks created by the stylus. The minimum normal stress necessary to orient the surface of the polyimide films was found to be 45 MPa, much lower than the bulk yield stress of 200–300 MPa [168].
- The surface composition of annealed PS/PBrS bilayer systems was characterized with PEEM and NEXAFS spectroscopy [65], revealing that PS is encapsulating the PBrS when the system is annealed. The morphology of annealed and un-annealed PS/PBrS blends and the influence of an attractive substrate on equilibrium morphologies were characterized [88,169]. It could be deduced that the surface tension of PBrS is 39% polar, that the dispersive contribution to the PBrS surface energy is less than 26 dyn/cm^2 [88] and that only partial encapsulation by PS occurs if the film thickness is less than R_g [169].
- Studies with NEXAF microscopy also comprised the morphological characterization of as-cast and annealed blends of PS/PMMA [84]. Quantitative lateral information or surface characterization allowed to infer a complete 3D picture in some systems that elucidated the complicated interplay between thin film constraints and interfacial energies [65,84]. Furthermore, a transition in the critical micelle concentration of PS-*b*-PMMA in PS/PMMA thin films as a function of confinement was observed [170]. PS-*b*-PMMA cannot easily form micelles if the film thickness is smaller than the bulk micelle size. This forces the block copolymer to the PS/PMMA interface in bilayer films and effectively emulsifies the bilayer at composition that would have little effect on a bulk material. The influence of substrates on the morphology [171,172] and the validity of the time–temperature superposition in thin PS/PMMA films were determined [90]. PS/PMMA thin films and their surfaces have also been used to study surface segregation [96,173], selective absorption of biopolymers [147] and their absorption kinetics and concentration dependence [78]. The thin film morphologies of phase-separated PS and polyvinylmethylether (PVME) [174], PS/poly(styrene acrylonitrile) [174], and PS/poly(*n*-butyl methacrylate) (P*n*BMA) thin film blends and possible encapsulation of one polymer by the other have also been determined [175].

Thin film polymer composites: the effects of modifiers and filler on the morphology of thin film blends have been characterized for a number of systems. Often, these studies are ultimately aimed at understanding bulk properties, but the sample preparation is simplified by casting films. However, the high shear present during casting might prevent a direct conclusion on how comparable effects can be achieved in the bulk. The comparison of the morphology of samples with and without the fillers allows conclusions to be drawn about the relative interfacial activity of various fillers and their ability to compatibilize incompatible blends. It was shown that methyl methacrylate/polyhedral oligomeric silsesquioxane random copolymers can significantly compatibilize PS/PMMA blends [176] and that surface modified clays accomplish the same in a number of polymer blends [177]. Functionalized WS_2 nanotubes were used to produce new PS/PMMA nanocomposites with dramatically reduced domain size so indicative of compatibilization [178]. Spun-cast elastomeric thin film composites based on the effects of carbon black and pyrogeneous silica fillers and a styrene–butadiene rubber (SBR) on the interfacial properties of polybutadiene (PB) and the terpolymer [brominated poly(isobutylene-*co*-*p*-methylstyrene) (BIMS)] have also been characterized with NEXAFS microscopy to complement neutron reflectivity, neutron small angle scattering and SPM studies [179,180]. Pyrogeneous silica has a less pronounced effect on the interfacial characteristics in these elastomeric blends. When both carbon and silica are incorporated into the PB layer, the effect of carbon black is offset by the silica fillers [180]. Furthermore, SBR is not fully miscible with BIMS and PB; the addition of a relatively small amount of SBR enhances the compatibilization of the PB/BIMS interface [179,180].

Bulk multicomponent, multiphasic polymers: in order to investigate bulk properties and bulk morphologies, thin sections produced by ultramicrotomy are investigated in transmission electron microscope.

- Blends and composites based on styrene–butadiene rubber (SBR) and butadiene rubber (BR) are widely used throughout the rubber and tire industry. The vast majority of these blends are heterogeneous on some length scale [181,182], which influences their mechanical properties. Furthermore, many high-performance materials have fillers and curatives added. Determining the polymer phase structure itself and the distribution of fillers and curatives in each of the elastomer phases is highly desirable in order to correlate the morphology to properties. Improvements are being sought continuously. For example, poly(isobutylene-*co*-4-bromomethylstyrene) (IMS) can be blended with highly unsaturated general-purpose rubbers to impart unique barrier or dynamic properties and enhanced oxidative stability [183]. The complex series of compounding, mixing and curing profoundly impacts the homogeneity of these materials. The characterization of the phase morphology of blends of commercial rubbers like polybutadiene (PB), PI, SBR and brominated poly(isobutylene-*co*-4-bromomethylstyrene) (BIMS) continues to represent a problem for conventional techniques, especially in the case of filled rubbers. Dias et al. [183] and Winesett et al. [184] have thus explored the utility of NEXAFS microscopy for these applications and found that the phase

morphology of various blends and the distribution of silica and carbon black fillers can be determined based on spectroscopic differences. The effects of SBR on the miscibility of PB and BIMS were investigated by Zhang et al. [179]. The results, including morphological characterization with NEXAFS microscopy, show that SBR enhances the compatibilization of the PB/BIMS blends. The effects of carbon black and silica on the interfacial properties of PB/BIMS blends have been investigated in related studies with neutron reflectivity, ultra-small angle neutron scattering, SPM and NEXAFS microscopy [180].

- In a related investigation focusing on the disposal of rubber blends, Smith et al. investigated alternative recycling strategies for tires; specifically, if highly dispersed blends of thermoplastics and tires can be produced with cryomilling [127]. NEXAFS microscopy of cryogenic mechanically alloyed tires revealed dispersion with sub-micron domains in PET and PMMA matrixes. The tire and thermoplastic materials did not appear to interact chemically within the sensitivity limits of NEXAFS. For the milling conditions employed, there was also no significant chemical interaction between constituent polymers in PI/tire/PMMA ternary blends. Based on the ability to produce good dispersion of the tire material, the results indicated that cryogenic mechanical alloying constitutes a potential alternative for recycling elastomeric materials.
- Sloop et al. characterized the modification of polycarbonate/poly(acrylonitrile/butadiene/styrene) blends containing TiO_2 fillers during recycling [185].
- Additional bulk, multicomponent materials characterized are: multilayer systems utilized for food packaging [186], the composition and dispersion of toner particles [187], and macrophase-separated random block copolymer/homopolymer blends [188].

Other organic macromolecular materials: characterization of the organic components of other materials, many of which are known or presumed to be macromolecular in nature, ranging from organic geochemical materials [189–191] to meteorites [192], coal [193–196], comets [197,198], wood [199], soils [200], and aerosol particles [201]. This list is not complete, but simply indicates that NEXAFS microscopy is a general characterization tool and that any carbonaceous material is a likely target to be characterized and one that will yield new information.

Appendix. Supplementary data

Supplementary data associated with this article can be found, in the online version, at doi:10.1016/j.polymer.2007.10.030.

References

[1] Paul DR, Bucknall CB, editors. Polymer blends, vols. I and II. New York: Wiley; 2000.
[2] Geoghegan M, Krausch G. Prog Polym Sci 2003;28:261.
[3] Walheim S, Boltau M, Mlynek J, Krausch G, Steiner U. Macromolecules 1997;30:4995.
[4] Bates FS, Fredrickson GH. Phys Today 1999;52:32.
[5] Ruzette AV, Leibler L. Nat Mater 2005;4:19.
[6] Thurn-Albrecht T, Schotter J, Kastle CA, Emley N, Shibauchi T, Krusin-Elbaum L, et al. Science 2000;290:2126.
[7] Stoykovich MP, Muller M, Kim SO, Solak HH, Edwards EW, de Pablo JJ, et al. Science 2005;308:1442.
[8] Mezzenga R, Ruokolainen J, Fredrickson GH, Kramer EJ, Moses D, Heeger AJ, et al. Science 2003;299:1872.
[9] Roe RJ. Methods of X-ray and neutron scattering in polymer science. New York: Oxford University Press; 2000.
[10] Jones RAL. Polymers at surfaces and interfaces. New York: Cambridge University Press; 1999.
[11] Ade H, Zhang X, Cameron S, Costello C, Kirz J, Williams S. Science 1992;258:972.
[12] Ade H, Hsiao B. Science 1993;262:1427.
[13] Wang C, Araki T, Ade H. Appl Phys Lett 2005;87:214109.
[14] Araki T, Ade H, Stubbs JM, Sundberg DC, Mitchell GJK, Kilcoyne ALD. Appl Phys Lett 2006;89:124106.
[15] Mitchell GE, Landes BG, Lyons J, Kern BJ, Devon MJ, Koprinarov I, et al. Appl Phys Lett 2006;89:044101.
[16] Ding YS, Hubbard SR, Hodgson KO, Register RA, Cooper SL. Macromolecules 1988;21:1698.
[17] Register RA, Cooper SL. Macromolecules 1990;23:318.
[18] Register RA, Cooper SL. Macromolecules 1990;23:310.
[19] Jark W, Russell TP, Comelli G, Stohr J. Thin Solid Films 1991;199:161.
[20] Stöhr J. NEXAFS spectroscopy. New York: Springer-Verlag; 1992.
[21] Kilcoyne ALD, Tyliszczak T, Steele WF, Fakra S, Hitchcock P, Franck K, et al. J Synchrotron Radiat 2003;10:125.
[22] Balta-Calleja FJ, Vonk CG. X-ray scattering of synthetic polymers. Amsterdam: Elsevier; 1989.
[23] Glatter O, Kratky O. Small angle X-ray scattering. New York: Academic Press; 1982.
[24] Seeck OH, Kaendler ID, Tolan M, Shin M, Rafailovich MH, Sokolov J, et al. Appl Phys Lett 2000;76:2713.
[25] Anastasiadis SH, Russell TP, Satija SK, Majkrzak CF. J Chem Phys 1990;92:5677.
[26] Fernandez ML, Higgins JS, Penfold J, Ward RC, Shackleton C, Walsh DJ. Polymer 1988;29:1923.
[27] Wang C, Araki T, Watts B, Harton S, Koga T, Basu S, et al. J Vac Sci Technol A 2007;25:575.
[28] Virgili JM, Tao YF, Kortright JB, Balsara NP, Segalman RA. Macromolecules 2007;40:2092.
[29] McNeill CR, Watts B, Thomsen L, Belcher WJ, Greenham NC, Dastoor PC. Nano Lett 2006;6:1202.
[30] Ade H, Smith AP, Cameron S, Cieslinski R, Mitchell G, Hsiao B, et al. Polymer 1995;36:1843.
[31] Ade H. NEXAFS microscopy. In: Kroschwitz J, editor. Encylcopedia of polymer science and technology. 3rd ed. Wiley. doi:10.1002/0471440264.pst403, http://www.mrw.interscience.wiley.com/epst/articles/pst403/frame.html; 2004.
[32] Ade H, Urquhart S. NEXAFS spectroscopy and microscopy of natural and synthetic polymers. In: Sham TK, editor. Chemical applications of synchrotron radiation. Singapore: World Scientific Publishing; 2002. p. 285.
[33] Kirz J, Jacobsen C, Howells M. Q Rev Biophys 1995;28:33.
[34] Howells M, Jacobsen C, Warwick T. Principles and applications of zone plate X-ray microscopes. In: Hawkes P, Spence J, editors. The science of microscopy. Kluwer Press; 2007.
[35] Henke BL, Gullikson EM, Davis JC. At Data Nucl Data Tables 1993;54:181.
[36] Attwood D. Soft X-rays and extreme ultraviolet radiation, principles and applications. Cambridge University Press; 2000.
[37] Saloman EB, Hubbell JH, Scofield JH. At Data Nucl Data Tables 1988;38:1.
[38] Hubbell JH, Gimm HA, Overbo I. J Phys Chem Ref Data 1980;9:1023.
[39] Urquhart SG, Ade H. J Phys Chem B 2002;106:8531.
[40] Lessard R, Cuny J, Cooper G, Hitchcock AP. Chem Phys 2007;331:289.
[41] Cooney RR, Urquhart SG. J Phys Chem B 2004;108:18185.
[42] Hitchcock AP, Mancini DC. J Electron Spectrosc Relat Phenom 1994;67:1.

[43] Kosugi N. Theor Chim Acta 1987;72:149.
[44] Kosugi N, Kuroda H. Chem Phys Lett 1980;74:490.
[45] Agren H, Yang L, Carravetta V, Pettersson LGM. Chem Phys Lett 1996; 259:21.
[46] Casida ME, Daul C, Goursot A, Koester A, Pettersson LGM, Proynov E, et al. DEMON-KS StoBe version. 1.0st ed. deMon Software; 2001.
[47] Hitchcock AP, Urquhart SG, Rightor EG. J Phys Chem 1992;96:8736.
[48] Urquhart SG, Hitchcock AP, Leapman RD, Priester RD, Rightor EG. J Polym Sci Part B Polym Phys 1995;33:1593.
[49] Urquhart SG, Hitchcock AP, Smith AP, Ade H, Rightor EG. J Phys Chem B 1997;101:2267.
[50] Urquhart SG, Hitchcock AP, Smith AP, Ade HW, Lidy W, Rightor EG, et al. J Electron Spectrosc Relat Phenom 1999;100:119.
[51] Cooper G, Gordon M, Tulumello D, Turci C, Kaznatcheev K, Hitchcock AR. J Electron Spectrosc Relat Phenom 2004;137–140:795.
[52] Smith AP, Ade H. Appl Phys Lett 1996;69:3833.
[53] Dhez O, Ade H, Urquhart S. J Electron Spectrosc Relat Phenom 2003; 128:85.
[54] Kaznacheyev K, Osanna A, Jacobsen C, Plashkevych O, Vahtras O, Agren H. J Phys Chem A 2002;106:3153.
[55] Zubavichus Y, Shaporenko A, Grunze M, Zharnikov M. J Phys Chem A 2005;109:6998.
[56] Anders S, Padmore HA, Duarte RM, Renner T, Stammler T, Scholl A, et al. Rev Sci Instrum 1999;70:3973.
[57] Schmidt T, Heun S, Slezak J, Diaz J, Prince KC, Lilienkamp G, et al. Surf Rev Lett 1998;5:1287.
[58] Feng J, Forest E, MacDowell AA, Marcus M, Padmore H, Raoux S, et al. J Phys Condens Matter 2005;17:S1339.
[59] Wichtendahl R, Fink R, Kuhlenbeck H, Preikszas D, Rose H, Spehr R, et al. Surf Rev Lett 1998;5:1249.
[60] Ade H, Kirz J, Hulbert SL, Johnson ED, Anderson E, Kern D. Appl Phys Lett 1990;56:1841.
[61] Ade HW. Nucl Instrum Methods Phys Res Sect A 1992;319:311.
[62] Shin HJ, Lee MK. Nucl Instrum Methods Phys Res Sect A 2001;467: 909.
[63] Marsi M, Casalis L, Gregoratti L, Günther S, Kolmakov A, Kovac J, et al. J Electron Spectrosc Relat Phenom 1997;84:73.
[64] Ade H, Kirz J, Hulbert S, Johnson E, Anderson E, Kern D. Nucl Instrum Methods Phys Res Sect A 1990;291:126.
[65] Ade H, Winesett DA, Smith AP, Anders S, Stammler T, Heske C, et al. Appl Phys Lett 1998;73:3775.
[66] Jacobsen C, Williams S, Anderson E, Brown MT, Buckley CJ, Kern D, et al. Opt Commun 1991;86:351.
[67] Warwick T, Franck K, Kortright J, Meigs G, Moronne M, Myneni S, et al. Rev Sci Instrum 1998;69:2964.
[68] Meyer-Ilse W, Attwood D, Koike M. The X-ray microscopy resource center at the advanced light source. In: Chance B, Deisenhober D, Ebashi S, et al., editors. Synchrotron radiation in biosciences. Oxford: Clarendon Press; 1994. p. 624.
[69] Nieman B, Rudolph D, Schmahl G. Appl Opt 1976;15:1883.
[70] Schmahl G, Rudolph D, Niemann B, Christ O. Q Rev Biophys 1980;13: 297.
[71] Anderson EH, Olynick DL, Harteneck B, Veklerov E, Denbeaux G, Chao WL, et al. J Vac Sci Technol B 2000;18:2970.
[72] Chao WL, Harteneck BD, Liddle JA, Anderson EH, Attwood DT. Nature 2005;435:1210.
[73] Spector S, Jacobsen C, Tennant D. J Vac Sci Technol B 1997;15:2872.
[74] Dejugnat C, Kohler K, Dubois M, Sukhorukov GB, Mohwald H, Zemb T, et al. Adv Mater 2007;19:1331.
[75] Winn B, Ade H, Buckley C, Howells M, Hulbert S, Jacobsen C, et al. Rev Sci Instrum 1996;67:A31.
[76] Winn B, Hao X, Jacobsen C, Kirz J, Miao J, Wirick S, et al. Optics for high-brightness synchrotron radiation beamlines II. In: SPIE proceedings, vol. 2856; 1996. p. 100.
[77] Jacobsen C, Wirick S, Flynn G, Zimba C. J Microsc 2000;197:173.
[78] Li L, Hitchcock AP, Robar N, Cornelius R, Brash JL, Scholl A, et al. J Phys Chem B 2006;110:16763.
[79] Wang J, Morin C, Hitchcock AP, Li L, Zhang X, Araki T, et al. Electron spectroscopy related phenomena, in press.
[80] Lanke UD, Haines B, Christensen E, Coulombe R, Stewart-Ornstein J, et al. 2006 Annual report. Canadian Light Source; 2007.
[81] De Stasio G, Perfetti L, Gilbert B, Fauchoux O, Capozi M, Perfetti P, et al. Rev Sci Instrum 1999;70:1740.
[82] Tonner BP, Dunham D, Droubay T, Kikuma J, Denlinger J, Rotenberg E, et al. J Electron Spectrosc Relat Phenom 1995;75:309.
[83] aXis2000 is written in Interactive Data Language (IDL). It is available free for non-commercial use from <http://unicorn.mcmaster.ca/aXis2000.html>.
[84] Ade H, Winesett DA, Smith AP, Qu S, Ge S, Sokolov J, et al. Europhys Lett 1999;45:526.
[85] Strang G. Linear algebra and its applications. San Diego: Harcourt Brace Jovanovich; 1988.
[86] Press WH, Flannery BP, Teukolsky SA, Vetterling WT. Numerical recipes in Fortran 77: the art of scientific computing. 2nd ed. Cambridge University Press; 1992.
[87] Zhang X, Balhorn R, Mazrimas J, Kirz J. J Struct Biol 1996;116: 335.
[88] Slep D, Asselta J, Rafailovich MH, Sokolov J, Winesett DA, Smith AP, et al. Langmuir 1998;14:4860.
[89] Winesett DA, Gersappe D, Rafailovich M, Sokolov J, Zhu S, Ade H. AIP Conf Proc Ser 2000;507:274.
[90] Winesett DA, Zhu S, Sokolov J, Rafailovich M, Ade H. High Perform Polym 2000;12:599.
[91] Dynes JJ, Tyliszczak T, Araki T, Lawrence JR, Swerhone GDW, Leppard GG, et al. Environ Sci Technol 2006;40:1556.
[92] Dynes JJ, Lawrence JR, Korber DR, Swerhone GDW, Leppard GG, Hitchcock AP. Sci Total Environ 2006;369:369.
[93] Lawrence JR, Swerhone GDW, Leppard GG, Araki T, Zhang X, West MM, et al. Appl Environ Microbiol 2003;69:5543.
[94] Hitchcock AP, Morin C, Heng YM, Cornelius RM, Brash JL. J Biomater Sci Polym Ed 2002;13:919.
[95] Felten A, Hody H, Bittencourt C, Pireaux JJ, Hernández Cruz D, Hitchcock AP. Appl Phys Lett 2006;89.
[96] Morin C, Ikeura-Sekiguchi H, Tyliszczak T, Cornelius R, Brash JL, Hitchcock AP, et al. J Electron Spectrosc Relat Phenom 2001;121:203.
[97] Hernández-Cruz D, Hitchcock AP, Tyliszczak T, Rousseau ME, Pezolet M. Rev Sci Instrum 2007;78.
[98] Hernández Cruz D, Rousseau ME, West MM, Pezolet M, Hitchcock AP. Biomacromolecules 2006;7:836.
[99] Rousseau ME, Hernández Cruz D, West MM, Hitchcock AP, Pezolet M. J Am Chem Soc 2007;129:3897.
[100] Kaznatcheev KV, Dudin P, Hitchcock AP. Phys Rev E, submitted for publication.
[101] Neuhausler U, Jacobsen C, Schulze D, Stott D, Abend S. J Synchrotron Radiat 1999;S55:1.
[102] Mitchell GE, Wilson LR, Dineen MT, Urquhart SG, Hayes F, Rightor EG, et al. Macromolecules 2002;35:1336.
[103] Stollberg H, Pokorny M, Hertz HM. J Microsc Oxford 2007;226:71.
[104] Schöll A, Fink R, Umbach E, Mitchell GE, Urquhart SG, Ade H. Chem Phys Lett 2003;370:834.
[105] Maser J, Osanna A, Wang Y, Jacobsen C, Kirz J, Spector S, et al. J Microsc 2000;197:68.
[106] Tzvetkov G, Graf B, Wiegner R, Raabe J, Quitmann C, Fink R. Micron 2007.
[107] Rightor EG, Hitchcock AP, Ade H, Leapman RD, Urquhart SG, Smith AP, et al. J Phys Chem B 1997;101:1950.
[108] Coffey T, Urquhart SG, Ade H. J Electron Spectrosc Relat Phenom 2002;122:65.
[109] Zhang X, Jacobsen C, Lindaas S, Williams S. J Vac Sci Technol B 1995; 13:1477.
[110] Beetz T, Jacobsen C. J Synchrotron Radiat 2003;10:280.
[111] Wang J, Stover HDH, Hitchcock AP, Tyliszczak T. J Synchrotron Radiat 2007;14:181.
[112] Underwood JH, Gullikson EM. J Electron Spectrosc Relat Phenom 1998;92:265.

[113] Ade H. X-ray spectromicroscopy. In: Samson JAR, Ederer DL, editors. Experimental methods in the physical science, vol. 32. Academic Press; 1998. p. 225.
[114] Ade H, Smith AP, Zhang H, Zhuang GR, Kirz J, Rightor E, et al. J Electron Spectrosc Relat Phenom 1997;84:53.
[115] Ade H. Trends Polym Sci 1997;5:58.
[116] Hitchcock AP, Koprinarov I, Tyliszczak T, Rightor EG, Mitchell GE, Dineen MT, et al. Ultramicroscopy 2001;88:33.
[117] Hitchcock AP. J Synchrotron Radiat 2001;8:66.
[118] Hitchcock AP, Stover HDH, Croll LM, Childs RF. Aust J Chem 2005; 58:423.
[119] Urquhart SG, Smith AP, Ade HW, Hitchcock AP, Rightor EG, Lidy W. J Phys Chem B 1999;103:4603.
[120] Rightor EG, Urquhart SG, Hitchcock AP, Ade H, Smith AP, Mitchell GE, et al. Macromolecules 2002;35:5873.
[121] Smith AP, Spontak RJ, Ade H, Smith SD, Koch CC. Adv Mater 1999; 11:1277.
[122] Smith AP, Bai C, Ade H, Spontak RJ, Balik CM, Koch CC. Macromol Rapid Commun 1998;19:557.
[123] Smith AP, Shay JS, Spontak RJ, Balik CM, Ade H, Smith SD, et al. Polymer 2000;41:6271.
[124] Smith AP, Ade H, Balik CM, Koch CC, Smith SD, Spontak RJ. Macromolecules 2000;33:2595.
[125] Smith AP, Ade H, Koch CC, Smith SD, Spontak RJ. Macromolecules 2000;33:1163.
[126] Smith AP, Ade H, Smith SD, Koch CC, Spontak RJ. Macromolecules 2001;34:1536.
[127] Smith AP, Ade H, Koch CC, Spontak RJ. Polymer 2001;42:4453.
[128] Smith AP, Spontak RJ, Koch CC, Smith SD, Ade H. Macromol Mater Eng 2000;274:1.
[129] Takekoh R, Okubo M, Araki T, Stover HDH, Hitchcock AP. Macromolecules 2005;38:542.
[130] Croll LM, Stover HDH, Hitchcock AP. Macromolecules 2005;38:2903.
[131] Koprinarov I, Hitchcock AP, Li WH, Heng YM, Stöver HDH. Macromolecules 2001;34:4424.
[132] Hitchcock AP, Li J, Reijerkerk S, Foley P, Stöver HDH, Shirley I. J Electron Spectrosc Relat Phenom 2007.
[133] Araki T, Hitchcock AP, Shen F, Chang PL, Wang M, Childs RF. J Biomater Sci Polym Ed 2005;16:611.
[134] Lerotic M, Jacobsen C, Gillow JB, Francis AJ, Wirick S, Vogt S, et al. J Electron Spectrosc Relat Phenom 2005;144–147:1137.
[135] Malinowski E. Factor analysis in chemistry. 2nd ed. New York: John H. Wiley & Sons; 1991.
[136] Croll LM, Stover HDH. Langmuir 2003;19:5918.
[137] Fujii S, Armes SP, Araki T, Ade H. J Am Chem Soc 2005;127:16808.
[138] Mitchell G. Personal communication.
[139] Araki T, Ade H, Fujii S, Armes SP, in preparation.
[140] Shaheen SE, Brabec CJ, Sariciftci NS, Padinger F, Fromherz T, Hummelen JC. Appl Phys Lett 2001;78:841.
[141] McNeill JD, O'Connor DB, Barbara PF. J Chem Phys 2000;112:7811.
[142] McNeill CR, Frohne H, Holdsworth JL, Furst JE, King BV, Dastoor PC. Nano Lett 2004;4:219.
[143] McNeill JD, Barbara PF. J Phys Chem B 2002;106:4632.
[144] McNeill CR, Watts B, Thomsen L, Belcher WJ, Kilcoyne ALD, Greenham NC, et al. Small 2006;2:1432.
[145] McNeill CR, Watts B, Thomsen L, Ade H, Greenham NC, Dastoor PC. Macromolecules 2007;40:3263.
[146] Watts B, Queen D, Kilcoyne ALD, Ade H, Hellman F. Abstracts of MRS Fall 2007 meeting; 2007.
[147] Morin C, Hitchcock AP, Cornelius RM, Brash JL, Urquhart SG, Scholl A, et al. J Electron Spectrosc Relat Phenom 2004;137–140:785.
[148] Li L, Brash J, Cornelius R, Hitchcock AP. J Phys Chem B, in press.
[149] Granick S, Kumar SK, Amis EJ, Antonietti M, Balazs AC, Chakraborty AK, et al. J Polym Sci Part B Polym Phys 2003;41:2755.
[150] Reiter G, Sommer JU. Phys Rev Lett 2001;87:226101.
[151] Wang Y, Ge S, Rafailovich M, Sokolov J, Zou Y, Ade H, et al. Macromolecules 2004;37:3319.
[152] Wang Y, Rafailovich M, Sokolov J, Gersappe D, Araki T, Zou Y, et al. Phys Rev Lett 2006;96:028303.
[153] Harton SE, Stevie FA, Ade H. Macromolecules 2006;39:1639.
[154] Wang C, Ade H, Harton SE. Macromolecules, in preparation.
[155] Miller RD. Science 1999;286:421.
[156] Stubbs JM, Sundberg DC. Polymer 2005;46:1125.
[157] Welch CF, Hjelm RP, Mang JT, Wrobleski DA, Orler EB, Hawley ME, et al. Polym Mater Sci Eng 2005;93:289.
[158] Williams S, Zhang X, Jacobsen C, Kirz J, Lindaas S, Vanthof J, et al. J Microsc Oxford 1993;170:155.
[159] Drake IJ, Liu TCN, Gilles M, Tyliszczak T, Kilcoyne ALD, Shuh DK, et al. Rev Sci Instrum 2004;75:3242.
[160] Guay D, Stewart-Ornstein J, Zhang XR, Hitchcock AP. Anal Chem 2005;77:3479.
[161] Van Waeyenberge B, Puzic A, Stoll H, Chou KW, Tyliszczak T, Hertel R, et al. Nature 2006;444:461.
[162] Johansson GA, Tyliszczak T, Mitchell G, Keefe M, Hitchcock AP. J Synchrotron Radiat, in press.
[163] Hitchcock AP, Johansson GA, Mitchell GE, Keefe MH, Tyliszcak T. Appl Phys Lett A, submitted for publication.
[164] Kirz J, Rarback H. Rev Sci Instrum 1985;56:1.
[165] Feser M, Carlucci-Dayton M, Jacobsen C, Kirz J, Neuhäusler U, Smith G, et al. Proc SPIE 1998;3449:19.
[166] Bluhm H, Andersson K, Araki T, Benzerara K, Brown GE, Dynes JJ, et al. J Electron Spectrosc Relat Phenom 2006;150:86.
[167] Kaznatcheev KV, Karunakaran C, Lanke UD, Urquhart SG, Obst M, Hitchcock AP. AIP Conf Proc, in press.
[168] Cossy-Favre A, Diaz J, Liu Y, Brown HR, Samant MG, Stöhr J, et al. Macromolecules 1998;31:4957.
[169] Slep D, Asselta J, Rafailovich MH, Sokolov J, Winesett DA, Smith AP, et al. Langmuir 2000;16:2369.
[170] Zhu S, Liu Y, Rafailovich MH, Sokolov J, Gersappe D, Winesett DA, et al. Nature 1999;400:49.
[171] Winesett DA, Ade H, Sokolov J, Rafailovich M, Zhu S. Polym Int 2000; 49:458.
[172] Winesett DA, Story S, Lüning J, Ade H. Langmuir 2003;19:8526.
[173] Harris M, Appel G, Ade H. Macromolecules 2003;36:3307.
[174] Cossy-Favre A, Diaz J, Anders S, Padmore H, Liu Y, Samant M, et al. Acta Phys Pol A 1997;91:923.
[175] Schmitt T, Guttmann P, Schmidt O, Müller-Buschbaum P, Stamm M, Schönhense G, et al. X-ray microscopy. AIP Conf Proc 1999;507:245.
[176] Zhang WH, Fu BX, Seo Y, Schrag E, Hsiao B, Mather PT, et al. Macromolecules 2002;35:8029.
[177] Si M, Araki T, Ade H, Kilcoyne ALD, Fisher R, Sokolov JC, et al. Macromolecules 2006;39:4793.
[178] Zhang W, Ge S, Wang Y, Rafailovich MH, Dhez O, Winesett DA, et al. Polymer 2003;44:2109.
[179] Zhang Y, Li W, Tang B, Ge S, Hu X, Rafailovich MH, et al. Polymer 2001;42:9133.
[180] Zhang YM, Ge S, Tang B, Koga T, Rafailovich MH, Sokolov JC, et al. Macromolecules 2001;34:7056.
[181] Roland CM. Rubber Chem Technol 1989;62:456.
[182] Hess WM, Herd CR, Vegvari PC. Rubber Chem Technol 1993;66:329.
[183] Dias J, Urquhart SG, Ade H, Stevens P. 155th Meeting of the rubber division. Chicago: American Chemical Society; 1999. paper no. 30.
[184] Winesett DA, Ade H, Smith AP, Urquhart SG, Dias AJ, Stevens P. Rubber Chem Technol 2003;76:803.
[185] Sloop CC, Ade H, Fornes RE, Gilbert RD, Smith AP. J Polym Sci Part B Polym Phys 2001;39:531.
[186] Smith AP, Urquhart SG, Winesett DA, Mitchell G, Ade H. Appl Spectrosc 2001;55:1676.
[187] Iwata N, Tani K, Watada A, Ikeura-Sekiguchi H, Araki T, Hitchcock AP. Micron 2006;37:290.
[188] Smith AP, Laurer JH, Ade HW, Smith SD, Ashraf A, Spontak R. Macromolecules 1997;30:663.
[189] Boyce CK, Cody GD, Feser M, Jacobsen C, Knoll AH, Wirick S. Geology 2002;30:1039.

[190] Boyce CK, Zwieniecki MA, Cody GD, Jacobsen C, Wirick S, Knoll AH, et al. Proc Natl Acad Sci USA 2004;101:17555.
[191] Boyce CK, Cody GD, Fogel ML, Hazen RM, Alexander CMO, Knoll AH. Int J Plant Sci 2003;164:691.
[192] Flynn GJ, Keller LP, Feser M, Wirick S, Jacobsen C. Geochim Cosmochim Acta 2003;67:4791.
[193] Botto RE, Cody GD, Kirz J, Ade H, Behal S, Disko M. Energy Fuels 1994;8:151.
[194] Cody GD, Botto RE, Ade H, Behal S, Disko M, Wirick S. Energy Fuels 1995;9:75.
[195] Cody GD, Botto RE, Ade H, Behal S, Disko M, Wirick S. Energy Fuels 1995;9:525.
[196] Cody GD, Botto RE, Ade H, Wirick S. Int J Coal Geol 1996;32:69.
[197] Sandford SA, Aleon J, Alexander CMO, Araki T, Bajt S, Baratta GA, et al. Science 2006;314:1720.
[198] Brownlee D, Tsou P, Aleon J, Alexander CMO, Araki T, et al. Science 2006;314:1711.
[199] Cody GD. AIP Conf Proc Ser 2000;507:307.
[200] Plaschke M, Rothe J, Schafer T, Denecke MA, Dardenne K, Pompe S, et al. Colloids Surf A 2002;197:245.
[201] Maria SF, Russell LM, Gilles MK, Myneni SCB. Science 2004;306:1921.

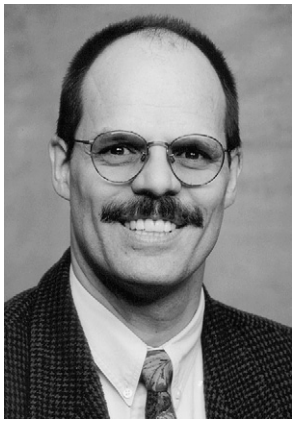

Harald Ade is a Professor of Physics at North Carolina State University. Educated at University of Tuebingen (Vordiplom) and SUNY at Stony Brook (Ph.D. in Physics, 1990), he joined the Faculty at North Carolina State University in 1992. Major awards include the K.F.J. Heinrich Award of the Microbeam Analysis Society (2000), an NSF Young Investigator Award (1994), and an R&D100 Award (1990). His research uses primarily synchrotron radiation based techniques for studies of a wide range of materials with an emphasis on polymeric materials.

Adam Hitchcock is a Professor of Chemistry and member of the Brockhouse Institute for Materials Research at McMaster University. Educated at McMaster (B.Sc. in Chemistry, 1974) and the University of British Columbia (Ph.D. in Chemical Physics, 1978), he joined the Faculty at McMaster in 1979. Major awards include the 1989 Noranda Lecture Award (Chemical Institute of Canada) and the senior Canada Research Chair in Materials Research CLS/CCRS (2001–2014). He was appointed as a fellow in Academies of the Royal Society of Canada in 2006. His research uses electron impact and synchrotron based techniques for studies of a wide range of materials.